



**HAL**  
open science

## **Detailed optical and near-infrared polarimetry, spectroscopy and broad-band photometry of the afterglow of GRB 091018: polarization evolution**

K. Wiersema, P. A. Curran, T. Krühler, A. Melandri, E. Rol, R. L. C. Starling, N. R. Tanvir, A. J. van Der Horst, S. Covino, J. P. U. Fynbo, et al.

### ► **To cite this version:**

K. Wiersema, P. A. Curran, T. Krühler, A. Melandri, E. Rol, et al.. Detailed optical and near-infrared polarimetry, spectroscopy and broad-band photometry of the afterglow of GRB 091018: polarization evolution. Monthly Notices of the Royal Astronomical Society, 2012, 426, pp.2-22. <10.1111/j.1365-2966.2012.20943.x>. <insu-03621705>

**HAL Id: insu-03621705**

**<https://insu.hal.science/insu-03621705v1>**

Submitted on 28 Mar 2022

HAL is a multi-disciplinary open access archive for the deposit and dissemination of scientific research documents, whether they are published or not. The documents may come from teaching and research institutions in France or abroad, or from public or private research centers.

L'archive ouverte pluridisciplinaire HAL, est destinée au dépôt et à la diffusion de documents scientifiques de niveau recherche, publiés ou non, émanant des établissements d'enseignement et de recherche français ou étrangers, des laboratoires publics ou privés.



Distributed under a Creative Commons CC BY 4.0 - Attribution - International License

# Detailed optical and near-infrared polarimetry, spectroscopy and broad-band photometry of the afterglow of GRB 091018: polarization evolution

K. Wiersema,<sup>1\*</sup> P. A. Curran,<sup>2</sup> T. Krühler,<sup>3</sup> A. Melandri,<sup>4,5</sup> E. Rol,<sup>6</sup> R. L. C. Starling,<sup>1</sup> N. R. Tanvir,<sup>1</sup> A. J. van der Horst,<sup>6</sup> S. Covino,<sup>4</sup> J. P. U. Fynbo,<sup>3</sup> P. Goldoni,<sup>7</sup> J. Gorosabel,<sup>8</sup> J. Hjorth,<sup>3</sup> S. Klose,<sup>9</sup> C. G. Mundell,<sup>5</sup> P. T. O’Brien,<sup>1</sup> E. Palazzi,<sup>10</sup> R. A. M. J. Wijers,<sup>6</sup> V. D’Elia,<sup>11,12</sup> P. A. Evans,<sup>1</sup> R. Filgas,<sup>13</sup> A. Gomboc,<sup>14,15</sup> J. Greiner,<sup>13</sup> C. Guidorzi,<sup>16</sup> L. Kaper,<sup>6</sup> S. Kobayashi,<sup>5</sup> C. Kouveliotou,<sup>17</sup> A. J. Levan,<sup>18</sup> A. Rossi,<sup>9</sup> A. Rowlinson,<sup>1,6</sup> I. A. Steele,<sup>5</sup> A. de Ugarte Postigo<sup>3,8</sup> and S. D. Vergani<sup>4</sup>

<sup>1</sup>University of Leicester, University Road, Leicester LE1 7RH

<sup>2</sup>Laboratoire AIM, CEA/IRFU-Université Paris Diderot-CNRS/INSU, CEA DSM/IRFU/SAP, Centre de Saclay, F-91191 Gif-sur-Yvette, France

<sup>3</sup>Dark Cosmology Centre, Niels Bohr Institute, University of Copenhagen, Juliane Maries Vej 30, 2100 Copenhagen, Denmark

<sup>4</sup>INAF – Osservatorio Astronomico di Brera, via E. Bianchi 46, I-23807 Merate, Italy

<sup>5</sup>Astrophysics Research Institute, Liverpool John Moores University, Twelve Quays House, Egerton Wharf, Birkenhead CH41 1LD

<sup>6</sup>Astronomical Institute ‘Anton Pannekoek’, University of Amsterdam, 1090 GE Amsterdam, the Netherlands

<sup>7</sup>Laboratoire Astroparticule et Cosmologie, 10 rue A. Domon et L. Duquet, 75205 Paris Cedex 13, France

<sup>8</sup>IAA – CSIC, Glorieta de la Astronomía s/n, 18008 Granada, Spain

<sup>9</sup>Thüringer Landessternwarte Tautenburg, Sternwarte 5, 07778 Tautenburg, Germany

<sup>10</sup>INAF – Istituto di Astrofisica Spaziale e Fisica Cosmica di Bologna, Via Gobetti 101, I-40129 Bologna, Italy

<sup>11</sup>INAF – Osservatorio Astronomico di Roma, via di Frascati 33, 00040 Monte Porzio Catone, Italy

<sup>12</sup>ASI-Science Data Center, via Galileo Galilei, 00044 Frascati, Italy

<sup>13</sup>Max-Planck-Institut für Extraterrestrische Physik, Giessenbachstraße 1, 85748 Garching, Germany

<sup>14</sup>Faculty of Mathematics and Physics, University of Ljubljana, Jadranska 19, SI-1000 Ljubljana, Slovenia

<sup>15</sup>Centre of Excellence SPACE-SI, Aškerčeva cesta 12, SI-1000 Ljubljana, Slovenia

<sup>16</sup>Physics Department, University of Ferrara, via Saragat 1, I-44122, Ferrara, Italy

<sup>17</sup>Space Science Office, VP62, NASA/Marshall Space Flight Center Huntsville, AL 35812, USA

<sup>18</sup>Department of Physics, University of Warwick, Coventry CV4 7AL

Accepted 2012 March 15. Received 2012 March 14; in original form 2012 February 10

## ABSTRACT

Follow-up observations of large numbers of gamma-ray burst (GRB) afterglows, facilitated by the *Swift* satellite, have produced a large sample of spectral energy distributions and light curves, from which their basic micro- and macro-physical parameters can in principle be derived. However, a number of phenomena have been observed that defy explanation by simple versions of the standard fireball model, leading to a variety of new models. Polarimetry can be a major independent diagnostic of afterglow physics, probing the magnetic field properties and internal structure of the GRB jets. In this paper we present the first high-quality multi-night polarimetric light curve of a *Swift* GRB afterglow, aimed at providing a well-calibrated data set of a typical afterglow to serve as a benchmark system for modelling afterglow polarization behaviour. In particular, our data set of the afterglow of GRB 091018 (at redshift  $z = 0.971$ ) comprises optical linear polarimetry ( $R$  band, 0.13–2.3 d after burst); circular polarimetry ( $R$  band) and near-infrared linear polarimetry ( $K_s$  band). We add to that high-quality optical and near-infrared broad-band light curves and spectral energy distributions as well as afterglow spectroscopy. The linear polarization varies between 0 and 3 per cent, with both long and short

\*E-mail: kw113@star.le.ac.uk

time-scale variability visible. We find an achromatic break in the afterglow light curve, which corresponds to features in the polarimetric curve. We find that the data can be reproduced by jet break models only if an additional polarized component of unknown nature is present in the polarimetric curve. We probe the ordered magnetic field component in the afterglow through our deep circular polarimetry, finding  $P_{\text{circ}} < 0.15$  per cent ( $2\sigma$ ), the deepest limit yet for a GRB afterglow, suggesting ordered fields are weak, if at all present. Our simultaneous *R*- and *Ks*-band polarimetry shows that dust-induced polarization in the host galaxy is likely negligible.

**Key words:** acceleration of particles – techniques: polarimetric – gamma-ray burst: individual: GRB 091018.

## 1 INTRODUCTION

Collimated outflows in the form of jets are ubiquitous, from active galactic nucleus jets driven by accretion of material by supermassive black holes in galactic centres to those associated with stellar sources such as X-ray binaries and galactic microquasars. A particularly exciting view of the fundamental physics of jet sources is offered by gamma-ray bursts (GRBs), which form the extreme end of the energy and Lorentz factor parameter space. Since the discovery of afterglows in 1997 (Costa et al. 1997; van Paradijs et al. 1997) we have a broad picture of the origin and cause of GRBs: through a catastrophic event (in the case of long-duration GRBs this is the core collapse of a massive star), a jet of highly relativistic material is ejected. In the standard fireball model (e.g. Mészáros & Rees 1997), the resulting broad-band emission detected from X-ray energies through to radio waves – the so-called afterglow – is explained by the relativistic ejecta colliding with the surrounding circumburst medium. The afterglow radiation we detect is consistent with a synchrotron emission (e.g. Mészáros & Rees 1992, 1997; Wijers & Galama 1999), characterized by a series of smoothly connected power laws, with characteristic break frequencies and fluxes. The macroscopic properties of shocks are largely understood, and the dynamics of the shock created when the relativistic jet hits the circumstellar matter can be written down in terms of the explosion energy, the density (and density gradient) of the medium into which the shock ploughs and the composition of the shocked material. However, outstanding questions remain on the nature of the *microphysics*: how are the relativistic particles that radiate the observed emission accelerated? Where does the magnetic field in the shocked region come from and what is its structure?

Since its launch in 2004, the *Swift* satellite (Gehrels et al. 2004) has provided us with hundreds of well-sampled X-ray and UV/optical afterglow light curves from seconds to months after burst (see Gehrels, Ramirez-Ruiz & Fox 2009 for a review). These light curves revealed complexity that was unexpected from pre-*Swift* light curves (Piran & Fan 2007); the standard fireball model has received a growing number of modifications, and the concept of a canonical light curve was introduced to explain the steep fades, plateau phases and multiple breaks in *Swift* X-ray light curves (Nousek et al. 2006). In particular, discrepancies between X-ray and optical light curves of GRB afterglows and the rich array of light curve morphology including extended plateaux, rebrightenings and flares challenge existing GRB models (see Piran & Fan 2007 for a review). Explanations for these features include complex jet structure, energy re-injection due to late-time central energy activity, variable microphysics and off-axis emission, with a combination of effects likely

in action in most afterglows. However, these model variations are in principle non-degenerate: linear and circular polarimetry have the ability to separate out the various models for the behaviour of the (early) afterglows in a completely independent way, as these models have different implications for the magnitude and orientation of the optical polarization, as well as for their time dependence (e.g. Rossi et al. 2004).

The ground-breaking discovery and interpretation of sudden achromatic steepening in light curves at  $\sim 1$  d post-burst in pre-*Swift* GRBs – so-called jet breaks – provided the first convincing evidence of highly collimated ejection (e.g. Rhoads 1997, 1999; Sari, Piran & Halpern 1999) and allowed jet opening angles and collimation-corrected energies to be derived (e.g. Frail et al. 2001). Jet breaks were expected to be ubiquitous in *Swift* light curves, but the added complexity and multiple breaks in these light curves have made jet breaks difficult to identify unambiguously (e.g. Curran et al. 2007a). In contrast, the linear polarization around the time of the jet break is predicted to have a unique signature (Ghisellini & Lazzati 1999; Sari 1999; Rossi et al. 2004): at early times a distant observer located slightly off-axis will see the afterglow as a ring-shaped source, which has strong polarization in the radial direction (assuming that the magnetic field is compressed in the plane normal to the motion, i.e. ordered in the plane of the shock). In the received light, integrated over the ring, the polarization will largely cancel out. However, as the fireball decelerates the size of the ring increases and at some point the edge of the jet is reached, at which point the polarization does not completely cancel out anymore and linear polarization is observed. As the ring expands further, the opposite edge of the jet is reached as well, giving rise to a second peak in the linear polarization curve. Therefore polarimetry provides a useful tool to unambiguously identify jet breaks from other light curve breaks, though measured polarization curves of GRB afterglows have in some cases shown puzzling features (see e.g. the cases of GRBs 030329 and 020405 discussed further in Section 4.1). In addition, the linear polarization properties probe jet internal structure, as different polarization properties are predicted for ‘uniform’ or ‘structured’ jet energy distributions (Rossi et al. 2004, see also Section 4.2.2).

It has been shown that if some fraction of the magnetic field in the shock has large-scale order, the light may also be circularly polarized (Matsumiya & Ioka 2003; Sagiv, Waxman & Loeb 2004). For the forward shock (in the ambient medium), most models predict 0.01–1 per cent circular polarization during the first day (e.g. Matsumiya & Ioka 2003), depending on the strength and order of the magnetic fields and the wavelength of observation. Part of this range is within reach of large telescopes, as we will demonstrate in Section 3.2.

In the *Swift* era few polarimetric measurements have been performed. Arguably the most successful have been the early-time linear polarization measurements of the afterglows of GRBs 060418 and 090102, performed with the RINGO polarimeter on the rapidly responding robotic Liverpool Telescope (Mundell et al. 2007; Steele et al. 2009), the latter GRB showing a linear polarization of 10 per cent just 190 s after burst. Steele et al. (2009) interpret the light curve properties and high degree of polarization in GRB 090102 – which was detected when emission from the reverse shock dominated the received optical light – as evidence for large-scale ordered magnetic fields in the expanding fireball. This detection of significant polarization at early times provides strong motivation for following the polarization properties of the fading afterglow for many hours or days after the GRB. However, late-time polarimetric observations of GRBs (see Lazzati 2006 for an overview) show that the combination of fading afterglow and low levels of polarization (few per cent) requires large telescopes to obtain polarimetric observations over multiple days to high precision ( $\lesssim 0.3$  per cent), using multiple filters to distinguish dust induced from intrinsic afterglow polarization. In this paper we present the first such data set for a *Swift* burst, and the most extensive polarimetric data set of any burst since GRB 030329 (Greiner et al. 2003).

This paper is the first in a series on the afterglow of GRB 091018. In this first paper we will describe our data set in detail and compare the observed polarization light curves with those of other (pre-*Swift*) bursts and theoretical models. In a forthcoming second paper (Wiersema et al. in preparation; hereafter called Paper 2) we will discuss the dust properties in GRB sightlines from a combination of multi-wavelength polarimetry, spectroscopy, host imaging and broad-band afterglow spectral energy distributions. In a third paper (Paper 3) we will model the afterglow physics of GRB 091018 in greater detail and fit the polarization data to more detailed models, in particular considering energy injection.

This paper is organized as follows: in Section 2 we describe the polarimetry, spectroscopy and broad-band photometry observations, the data reduction and data calibration techniques; in Section 3 we discuss the detected features in the data and in Section 4 we compare the data to models and previous studies of afterglow polarimetric light curves. Throughout this paper we adopt a cosmology with  $H_0 = 71 \text{ km s}^{-1} \text{ Mpc}^{-1}$ ,  $\Omega_m = 0.27$ ,  $\Omega_\Lambda = 0.73$ .

## 2 OBSERVATIONS

GRB 091018 triggered the Burst Alert Telescope (BAT) on board the *Swift* satellite at 20:48:19 UT on 2009 October 18 (trigger 373172; Stamatikos et al. 2009). The prompt emission shows the burst to likely belong to the class of long bursts (Kouveliotou et al. 1993), with a duration of  $T_{90} = 4.4 \pm 0.6 \text{ s}$  (Markwardt et al. 2009; Ukwatta et al. 2012 report a spectral lag of  $143 \pm 297 \text{ ms}$ ). An X-ray and optical afterglow were found by the *Swift*X-Ray Telescope (XRT) and UV–Optical Telescope (UVOT). Chen et al. (2009) reported an afterglow redshift of 0.971 shortly after. Based on the initial brightness of the UVOT afterglow we activated our Very Large Telescope (VLT) polarimetry programme (programme 084.D-0949, PI: Wiersema).

### 2.1 R-band linear and circular polarimetry

#### 2.1.1 Data acquisition

We acquired imaging polarimetry using the Focal Reducer and low dispersion Spectrograph (FOR2) mounted on Unit Telescope 1

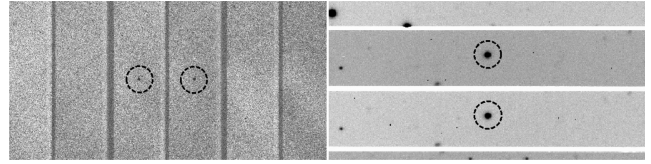


**Figure 1.** Small sections of data frames from the Infrared Spectrometer and Array Camera (ISAAC) *Ks*-band polarimetry (Left; angle 0 frame from *linK1*, see Section 2.2) and optical FOR2 polarimetry (right; angle  $-45^\circ$  from circular polarimetry epoch *cir1*). The circles are 5 arcsec in radius in each image and show the source in the *o* and *e* beams.

(Antu) of the VLT, using the FOR2  $R_{\text{special}}$  filter. After passing through a half or quarter wavelength plate (in the case of linear and circular polarimetry, respectively), a Wollaston prism splits the incoming light into an ordinary and extraordinary beam (hereafter the *o* and *e* beams) that are perpendicularly polarized. These *o* and *e* beams are imaged simultaneously, using a mask to avoid overlap of the two beams on the chip, as shown in Fig. 1. For each linear polarization data set we used four rotation angles of the half wavelength plate of 0, 22.5, 45 and 67.5. The circular polarization data were taken with  $-45^\circ$  and  $+45^\circ$  angles of the quarter wavelength plate.

To ensure relatively homogeneous polarimetric uncertainties as a function of time, exposure time was increased as the source faded. We employed a small dithering pattern, while taking care not to position the afterglow too close to the edges of the mask. We acquired a total of 20 linear polarization series and four circular polarization series, see Table 1.

We began our FOR2 polarimetric monitoring with a single short sequence of linear polarimetry. After this, to make full use of the brightness of the afterglow we switched to circular polarimetry, for which the models predict a much lower degree of polarization, requiring a large number of detected photons. Directly following the circular polarization, we continued our linear polarimetry. We obtained a further six sequences, and a further two at the end of the night. The next night we obtained further data sets at the beginning and the end of the night. A last, deep, point was obtained in the third night. Note that for all FOR2 polarimetry we position the afterglow close to the centre of the FOR2 field of view, on chip 1, where instrumental polarization is very low (well below our statistical errors, Patat & Romaniello 2006).

#### 2.1.2 Data reduction and calibration

We bias and flat field corrected all data using tasks in IRAF and using standard twilight sky flats. We use our own software in combination with IRAF routines to perform aperture photometry on the *o* and *e* images of the afterglow to find the source fluxes  $f_o$  and  $f_e$ , using the same approach as Rol et al. (2003). We used a seeing matched aperture of 1.5 times the on-frame full width at half-maximum (FWHM) of the point spread function (PSF), fitted per frame independently for the *o* and *e* as small differences in PSF shape may occur between the *o* and *e* beams, particularly for objects far off-axis. The sky subtraction was done using an annulus of inner and outer radii three and four times the FWHM. We measure  $f_o$  and  $f_e$  for all point-like objects in all frames.

We express the polarimetry information in terms of the Stokes vector  $\mathbf{S} = (Q, U, V, I)$  (see e.g. Chandrasekhar 1960), where the components of this vector have the following meaning:  $Q$  and  $U$  contain the behaviour of the linear polarization;  $V$  the circular polarization and  $I$  is the intensity. Generally we will use the

**Table 1.** Log of our polarimetric observations. The ID column gives a label to each polarimetric data set to make discussion easier, with linear polarimetry data sets labelled ‘lin’ and circular polarimetry ‘cir’. The exposure time is the exposure time per retarder angle (four angles for linear, two for circular polarimetry). The  $Q/I$  and  $U/I$  values are as measured: to obtain values corrected for scattering on Galactic dust, subtract the values derived in Section 2.1.3.

ID	$T - T_0$ (mid; d)	Exposure time (s)	FORS2, $R_{\text{special}}$		
			$Q/I$	$U/I$	$V/I$
<i>lin1</i>	0.131 89	180.0	$-0.0014 \pm 0.0009$	$-0.0036 \pm 0.0009$	
<i>cir1</i>	0.143 02	300.0			$-0.0005 \pm 0.0014$
<i>cir2</i>	0.151 33	300.0			$0.0011 \pm 0.0015$
<i>cir3</i>	0.159 64	300.0			$0.0003 \pm 0.0015$
<i>cir4</i>	0.167 95	300.0			$-0.0017 \pm 0.0015$
<i>lin2</i>	0.180 43	240.0	$0.0009 \pm 0.0009$	$-0.0040 \pm 0.0009$	
<i>lin3</i>	0.197 01	300.0	$-0.0012 \pm 0.0008$	$0.0024 \pm 0.0008$	
<i>lin4</i>	0.212 82	300.0	$0.0010 \pm 0.0009$	$-0.0023 \pm 0.0009$	
<i>lin5</i>	0.230 30	300.0	$-0.0006 \pm 0.0009$	$-0.0037 \pm 0.0009$	
<i>lin6</i>	0.246 11	300.0	$0.0083 \pm 0.0009$	$-0.0039 \pm 0.0009$	
<i>lin7</i>	0.263 57	300.0	$0.0056 \pm 0.0009$	$-0.0025 \pm 0.0009$	
<i>lin8</i>	0.279 36	300.0	$0.0057 \pm 0.0009$	$-0.0063 \pm 0.0009$	
<i>lin9</i>	0.454 83	300.0	$0.0119 \pm 0.0012$	$-0.0025 \pm 0.0012$	
<i>lin10</i>	0.470 64	300.0	$0.0067 \pm 0.0012$	$-0.0009 \pm 0.0012$	
<i>lin11</i>	1.139 40	300.0	$-0.0162 \pm 0.0023$	$0.0078 \pm 0.0023$	
<i>lin12</i>	1.155 22	300.0	$-0.0167 \pm 0.0022$	$0.0260 \pm 0.0023$	
<i>lin13</i>	1.173 45	300.0	$0.0088 \pm 0.0023$	$0.0130 \pm 0.0023$	
<i>lin14</i>	1.189 26	300.0	$-0.0123 \pm 0.0023$	$-0.0147 \pm 0.0023$	
<i>lin15</i>	1.207 29	300.0	$-0.0070 \pm 0.0024$	$-0.0054 \pm 0.0024$	
<i>lin16</i>	1.223 10	300.0	$-0.0126 \pm 0.0024$	$-0.0080 \pm 0.0024$	
<i>lin17</i>	1.360 06	600.0	$0.0022 \pm 0.0018$	$-0.0056 \pm 0.0018$	
<i>lin18</i>	1.391 83	600.0	$0.0014 \pm 0.0018$	$0.0057 \pm 0.0019$	
<i>lin19</i>	1.449 26	600.0	$-0.0141 \pm 0.0019$	$-0.0031 \pm 0.0019$	
<i>lin20</i>	2.390 23	720.0	$0.0111 \pm 0.0023$	$-0.0092 \pm 0.0023$	
			ISAAC, $K_s$		
<i>linK*</i>	0.4309	720.0 <sup>a</sup>	$0.0204 \pm 0.0078$	$0.0008 \pm 0.0083$	

<sup>a</sup>Combined value of three complete series (see Section 2.2).

normalized Stokes parameters  $q = Q/I$ ,  $u = U/I$  and  $v = V/I$  in this paper. Theoretical models are often expressed in terms of the polarization degree  $P$  and polarization angle  $\theta$ . These quantities can be found from the Stokes parameters through the relations

$$P_{\text{lin}} = \frac{\sqrt{Q^2 + U^2}}{I}$$

$$\theta = \frac{1}{2} \arctan(U/Q) + \phi$$

$$P_{\text{cir}} = V/I.$$

Constant  $\phi$  is an offset defined so that the resulting angle  $\theta$  conforms to the standard definitions of position angle (angle from north, counterclockwise, see Fig. 2):

$$\phi = \begin{cases} 0^\circ & \text{if } Q > 0 \text{ and } U \geq 0; \\ 180^\circ & \text{if } Q > 0 \text{ and } U < 0; \\ 90^\circ & \text{if } Q < 0. \end{cases}$$

Note that the conversion from Stokes parameters to  $P$  brings with it complications, discussed further below, so wherever possible we will work in Stokes parameter space.

To measure the Stokes  $Q/I$  and  $U/I$  parameters a measurement at two rotation angles suffices, but this introduces substantial systematic uncertainties, caused by imperfect flat fielding, imperfect

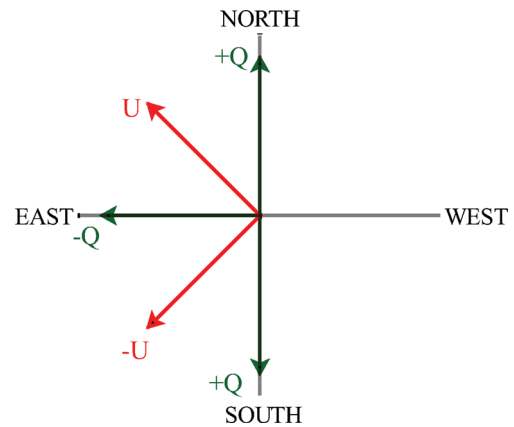


**Figure 2.** Coordinate definitions used in this paper.

background subtraction and imperfect behaviour of the half wavelength plate and Wollaston prism. Using four rotation angles with a constant stepsize (in this case of  $22.5^\circ$ ) means that several of these systematic effects cancel out (in particular the effects of background subtraction and flat fielding), leading to greatly improved polarimetric error terms. With these angles one can write (Patat & Romaniello

2006)

$$q = Q/I = \frac{2}{N} \sum_{i=0}^{N-1} F_i \cos(i\pi/2) \text{ and}$$

$$u = U/I = \frac{2}{N} \sum_{i=0}^{N-1} F_i \sin(i\pi/2),$$

where  $N$  is the number of half wavelength plate positions, and  $F_i$  is the normalized flux difference of a source in the  $o$  and  $e$  beams at the  $i$ th angle,

$$F_i = (f_{o,i} - f_{e,i}) / (f_{o,i} + f_{e,i}) = (f_{o,i} - f_{e,i}) / I.$$

For the circular polarimetry, taken with two angles of the retarder, we can simply write

$$v = V/I = \frac{1}{2} (F_{45} - F_{-45}).$$

After measurement of the fluxes of the sources in the images we compute their observed Stokes parameters and their uncertainties using the expressions above. The afterglow is always positioned on nearly the same position on CHIP1 (barring a small dither of  $\sim 16$  pixels in the  $Y$  direction in some epochs), on the optical axis. As such we expect the instrumental linear polarization to be negligible; see Patat & Romaniello (2006) for a thorough error analysis of FORS1, whose polarimetry optics were moved to the FORS2 instrument in 2009. Additionally, circular polarimetry Stokes  $V/I$  has no instrumental polarization on axis. In conclusion, the values of the Stokes parameters found through the methods above allow an investigation of the time dependence of the afterglow  $q$ ,  $u$  and  $v$ .

Theoretical models are generally expressed in terms of the linear and circular polarization fractions  $P_{\text{lin}}$  and  $P_{\text{cir}}$ , and we therefore convert the Stokes parameter information to these quantities using the equations above. We note that the uncertainty on the linear polarization angle is a function of the intrinsic polarization degree ( $\sigma_\theta = \sigma_{P_{\text{lin}}}/2P_{\text{lin}}$ ), which means that for the low polarization values and faint fluxes of afterglows the uncertainties in  $\theta$  are very large. Finally, the position angles found are corrected for the instrumental zero angle offset, which is  $-1^\circ.48$  at 655 nm (the central wavelength of the filter).<sup>1</sup>

Errors on  $q$  and  $u$  are generally distributed as a Normal distribution and the Stokes parameters can have positive and negative values. In contrast,  $P_{\text{lin}}$  is a positive definite quantity. As demonstrated in Simmons & Stewart (1985) (their Section 2), integrating the equation for the distribution of measured  $(P, \theta)$  over  $\theta$  shows that  $P_{\text{lin}}$  follows a Rice probability distribution rather than a Gaussian one. Directly using the equations above will lead to overestimated  $P_{\text{lin}}$  and incorrect confidence intervals, an effect generally referred to as the linear polarization bias. The correction to the resulting  $P_{\text{lin}}$  and associated confidence ranges has been studied through both analytical and numerical (Monte Carlo) methods. Generally speaking, this correction depends on  $\sigma_P$ ,  $P$  and the signal-to-noise ratio (SNR) of  $f_e + f_o$  (i.e. the SNR of  $I_i$ ). In the literature one often sees the Wardle & Kronberg (1974) prescription used, in which the input  $P$  values are multiplied by  $\sqrt{1 - (\sigma_P/P)^2}$  to find the bias-corrected polarization. We follow Sparks & Axon (1999) in using a parameter  $\eta = P \times \text{SNR}_F$  to trace the expected behaviour of the bias and  $\sigma_P$ : when  $\eta > 2$  the Wardle & Kronberg correction is valid, and  $\sigma_P$  is as computed directly from the uncertainty of  $F$ . In our FORS2 data set before correction for Galactic polarization (Section 2.1.3) all

data points have  $\eta > 2$ , and the bias correction is in all cases small compared to  $\sigma_P$ .

### 2.1.3 Polarization induced by the Galactic interstellar medium

To bring the afterglow  $q$  and  $u$  to an absolute frame, we need to correct for the linear polarization induced by scattering on dust in our Galaxy (Galactic interstellar polarization, GIP). Note that  $V/I$  does not require a correction as there is no circular GIP and the resulting linear polarization is much smaller than the threshold for noticeable linear–circular crosstalk (Patat & Romaniello 2006).

We assume here that the average intrinsic polarization of a sufficiently large sample of field stars is zero, that the bulk of the polarizing dust is between these stars and the observer and that therefore the observed distribution of  $q$  and  $u$  of field sources measures the GIP. We measure the Stokes  $q$  and  $u$  values of all sources that have an SNR above 20 in the FORS2 field, on both chips and in all epochs. A large number of artefacts are visible in our FORS2 imaging polarimetry, which have the appearance of a group of stars, and which are likely caused by reflections at the retarder plate;<sup>2</sup> we take special care to avoid stars close to these artefacts.

We then eliminate sources that appear significantly extended (galaxies), which may give spurious linear polarimetric signals if seeing conditions change during a polarimetric sequence. We further eliminate sources that are close to the mask edges and sources that are close to saturation in one or more of the images.

It is well known that FORS1, whose polarimetric optics are now cannibalized in FORS2, displayed a roughly radial instrumental linear polarization pattern, with polarization magnitude depending on the radial distance to the optical axis (see Patat & Romaniello 2006). The shape of the linear polarization pattern and its magnitude depend on the wavelength, and was found to reach nearly  $\sim 1.5$  per cent at the edges of the field of view (Patat & Romaniello 2006). While this effect is well calibrated for FORS1 in the  $V$  and  $I$  bands, a similar analysis has not yet been performed for FORS2. We therefore use a conservative approach and choose only stars close (radially) to the GRB position. It is of some importance to select not only the brightest stars (which would give smallest uncertainty in the GIP value), as this may result in a bias towards the nearest stars (in distance), and therefore may not sample the complete Galactic dust column towards the GRB. We also make sure that stars are selected with a fairly uniform distribution over the field (in terms of position angle).

We determine the GIP  $q$  and  $u$  values using three methods: we find the weighted mean of the field star distribution; we fit one-dimensional Gaussian curves on the histograms of the  $q$  and  $u$  distributions and we fit a two-dimensional Gaussian function (with its orientation as a free parameter) on the  $(q, u)$  distribution after converting this to a two-dimensional histogram (where a range of bin sizes are used based on the number of input data points). We perform these fits for a range of limit values on the maximum radial distance  $r$  between the input stars and the GRB, and on the maximum allowed  $\sigma_P$  of the stars. Unfortunately there are only a small number of fairly bright stars near to the GRB position, making it necessary to use a large limit on the radial distance to obtain a sufficient number of data points. We find a best balance between the number of sources in the fit and the uncertainties on the resulting  $q_{\text{GIP}}$  and  $u_{\text{GIP}}$  for limits  $\sigma_P \lesssim 0.35$  per cent and  $r \lesssim 2.0$  arcmin (103

<sup>1</sup> Tabulated at the FORS instrument webpages.

<sup>2</sup> [http://www.eso.org/observing/dfo/quality/FORS2/qc/problems/problems\\_fors2.html](http://www.eso.org/observing/dfo/quality/FORS2/qc/problems/problems_fors2.html)

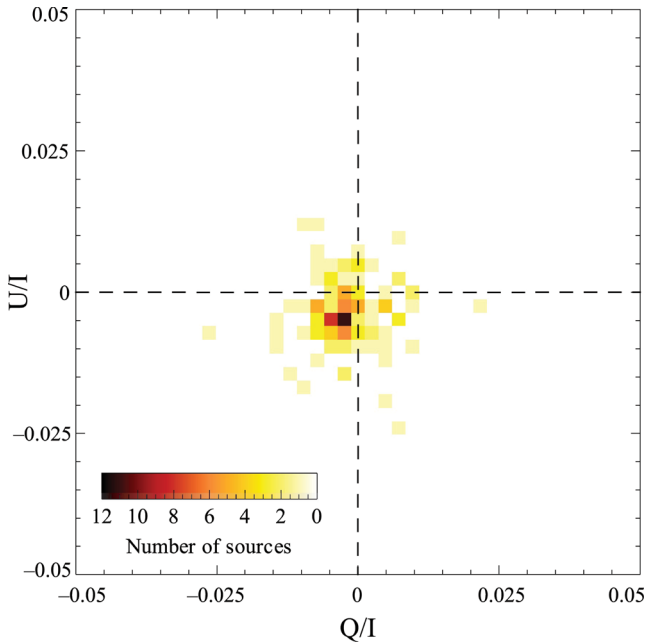


**Figure 3.** Measurements of  $q$  and  $u$  of field stars to determine the contribution to the received polarization by scattering on dust within our Galaxy. The dashed lines indicate  $q = 0$  and  $u = 0$ . Binsize used in this plot is 0.0025.

data points). Note that  $r = 2$  arcmin would correspond to  $\sim 0.23$  and  $\sim 0.34$  per cent instrumental polarization in the  $V$  and  $I$  bands in FORS1, respectively (Patat & Romaniello 2006). Using these limits the three methods give very similar GIP values. In Fig. 3 the distribution of data points (103 points) is shown. We find  $q_{\text{GIP}} = -0.0028$  and  $u_{\text{GIP}} = -0.0036$ , or  $P_{\text{GIP}} = 0.45$  per cent,  $\theta_{\text{GIP}} = 116^\circ$ . The two-dimensional fit gives the width of the Gaussian along the  $q$  axis as  $\sigma_q = 0.0030$  and along the  $u$  axis as  $\sigma_u = 0.0025$ , and the rotation of the containment ellipse from the  $q$  axis in radians, counter-clockwise, as  $\Theta = 1.7$  rad. The evidence for deviation from radial symmetry is not very strong, but the analysis of Patat & Romaniello (2006) shows that the FORS1 off-axis polarization pattern exhibited non-radial behaviour in the  $B$  band. We use this ellipse as a conservative error in the GIP Stokes parameters, following Rol et al. (2003). The fairly large uncertainty in these is likely dominated by the contribution of the unknown instrumental polarization pattern and the low number of bright stars within  $\sim 1$  arcmin of the GRB position.

The empirical relation  $P_{\text{GIP}} \lesssim 0.09E(B - V)$  (Serkowski, Matheson & Ford 1975) gives  $P_{\text{GIP}} \sim 0.3$  per cent, which compares well with the value derived above.

We now subtract from the GRB  $q$  and  $u$  values the  $q_{\text{GIP}}$  and  $u_{\text{GIP}}$  found above, to remove the (constant in time) component to the polarization caused by the Galactic interstellar medium (ISM). We propagate the errors on the GIP Stokes parameters into the resulting corrected values  $q_{\text{GIPcorr}}$  and  $u_{\text{GIPcorr}}$ . As is clear from Table 1, the afterglow polarization at very early times (e.g. *lin1*, *lin3*) all but vanishes, indicating that at early times the detected polarization is dominated by GIP. In many epochs, the  $q_{\text{GIPcorr}}$  and  $u_{\text{GIPcorr}}$  errors are dominated by the uncertainties in the GIP Stokes parameters. We compute GIP-corrected values for the polarization and position angle, which will bring the measured values on to an absolute scale. It is clear that the errors  $\sigma_P$  are increased dramatically, while  $P$  decreases in several epochs (to near zero in e.g. *lin1*), i.e. a drop in

**Table 2.** Linear polarization values, where coordinate definitions are used as in Fig. 2. All values have been corrected for polarization bias (after correction for GIP in the case of the last two columns), see Section 2.1.3. The uncertainties in the GIP  $q$ ,  $u$  value are fully propagated and dominate the uncertainties in the GRB afterglow GIP-corrected  $q$ ,  $u$ . The GIP-corrected polarization is very low (with inferred values of zero in two cases), and as such the errors on  $\theta$  are very large (as  $\sigma_\theta$  is a function of  $1/P$ , see Section 2.1.2).

ID	$P_{\text{lin}}$ (per cent)	$\theta$ (degrees)	$P_{\text{lin,GIPcorr}}$ (per cent)	$\theta_{\text{GIPcorr}}$ (degrees)
<i>lin1</i>	$0.36 \pm 0.13$	$126.1 \pm 19.3$	0 (0.32) <sup>b</sup>	
<i>lin2</i>	$0.38 \pm 0.12$	$143.1 \pm 17.7$	$0.21 \pm 0.31$	$177.0 \pm 47.5$
<i>lin3</i>	$0.24 \pm 0.11$	$60.2 \pm 25.1$	$0.56 \pm 0.27$	$37.7 \pm 24.7$
<i>lin4</i>	$0.22 \pm 0.12$	$148.5 \pm 28.4$	$0.26 \pm 0.31$	$9.2 \pm 43.7$
<i>lin5</i>	$0.35 \pm 0.12$	$132.1 \pm 19.0$	0 (0.32) <sup>b</sup>	
<i>lin6</i>	$0.90 \pm 0.12$	$168.9 \pm 7.9$	$1.07 \pm 0.30$	$179.2 \pm 16.1$
<i>lin7</i>	$0.59 \pm 0.12$	$169.5 \pm 12.0$	$0.78 \pm 0.31$	$3.9 \pm 21.2$
<i>lin8</i>	$0.84 \pm 0.13$	$157.4 \pm 8.8$	$0.84 \pm 0.30$	$171.1 \pm 19.9$
<i>lin9</i>	$1.20 \pm 0.17$	$175.5 \pm 8.1$	$1.44 \pm 0.32$	$2.2 \pm 12.6$
<i>lin10</i>	$0.65 \pm 0.17$	$177.7 \pm 14.7$	$0.94 \pm 0.32$	$8.0 \pm 18.6$
<i>lin11</i>	$1.77 \pm 0.32$	$78.6 \pm 10.2$	$1.73 \pm 0.36$	$69.8 \pm 11.7$
<i>lin12</i>	$3.07 \pm 0.32$	$62.8 \pm 5.9$	$3.25 \pm 0.35$	$57.6 \pm 6.1$
<i>lin13</i>	$1.53 \pm 0.32$	$29.5 \pm 11.9$	$1.99 \pm 0.35$	$27.6 \pm 10.0$
<i>lin14</i>	$1.89 \pm 0.32$	$116.4 \pm 9.8$	$1.42 \pm 0.36$	$114.6 \pm 14.0$
<i>lin15</i>	$0.81 \pm 0.33$	$110.2 \pm 21.7$	$0.27 \pm 0.38$	$101.6 \pm 47.1$
<i>lin16</i>	$1.45 \pm 0.33$	$107.7 \pm 13.0$	$1.00 \pm 0.38$	$102.2 \pm 20.2$
<i>lin17</i>	$0.54 \pm 0.25$	$147.0 \pm 24.0$	$0.41 \pm 0.34$	$168.8 \pm 36.6$
<i>lin18</i>	$0.52 \pm 0.26$	$39.5 \pm 25.3$	$0.97 \pm 0.32$	$32.8 \pm 17.8$
<i>lin19</i>	$1.42 \pm 0.27$	$97.6 \pm 10.7$	$1.08 \pm 0.35$	$88.7 \pm 17.9$
<i>lin20</i>	$1.40 \pm 0.32$	$161.6 \pm 13.1$	$1.45 \pm 0.37$	$169.0 \pm 14.3$
<i>linK</i> <sup>a</sup>	$2.0 \pm 0.8$	$10.9 \pm 20.9$	$2.0 \pm 0.8$	$10.9 \pm 20.9$

<sup>a</sup>Combined value from *linK1*, *linK2* and *linK3*. The GIP correction in the  $K$  band is more than an order of magnitude smaller than the statistical error in the polarization, so no correction is made. <sup>b</sup>See Simmons & Stewart (1985) for the probability of correctly inferring true polarization  $p_0 = 0$  from measured polarizations  $P$  using a maximum likelihood estimator. The number in parentheses is the 67 per cent confidence interval boundary.

$P/\sigma_P$ . At the same time, the statistical detection signal to noise (i.e. SNR of  $I_i$ , simply referred to as SNR in Section 2.1.2) stays the same. As the polarization bias is a function of both SNR and  $P/\sigma_P$ , the polarization bias correction is much larger in several epochs after GIP correction, showing the necessity of treating GIP effects in  $q$ ,  $u$  space rather than  $P$ ,  $\theta$  space in low polarization regimes. In several cases the Wardle & Kronberg prescription is not valid (see Simmons & Stewart 1985), and we use the methods recommended by Simmons & Stewart (1985) for low  $P/\sigma_P$  situations (which use a maximum likelihood estimator; this estimator has the lowest bias factor and lowest risk function values in this signal-to-noise range). In two cases this led to robust zero polarization values. We refer to Simmons & Stewart (1985) for a discussion on the probability of correctly inferring zero polarization for different estimators.

All resulting values are listed in Table 2.

## 2.2 K-band linear polarimetry

### 2.2.1 Data acquisition

We obtained an imaging polarimetry data set using the short-wave polarization (SWP) mode of the ISAAC instrument mounted on Unit Telescope 3 (Melipal) of the VLT, using the  $K_s$  filter. Observations coincided in part with  $R$ -band linear polarimetry, see Table 1.

ISAAC SWP mode uses a similar approach to FORS2 to obtain polarimetry: a Wollaston prism is inserted in the light path, and the incoming light is split into an ordinary and extraordinary beam (the  $o$  and  $e$  beam) that are perpendicularly polarized. The  $o$  and  $e$  beams are imaged simultaneously, using a mask to avoid overlap. The angular separation of the  $o$  and  $e$  images is wavelength dependent. The main difference between ISAAC and FORS2 imaging polarimetry is that a half wavelength plate is not present in ISAAC, requiring rotation of the instrument to obtain observations at the necessary angles, and the location of ISAAC in the Nasmyth focus.

At each instrument angle we use integration times of  $4 \times 15$  s, executed four times with significant dithering to facilitate sky subtraction. Because of the aperture mask, less than half of the field of view is visible at any given rotation angle, and one generally uses a dither pattern designed to sample the entire field. However, as the afterglow is faint and polarization low, we dither such that the afterglow always stays within the mask opening. After these  $4 \times 60$  s exposures, the instrument is rotated, and observations are repeated for the new position angle. By mistake we employed cumulative rotation offsets of 0, 22.5, 22.5 and 22.5. As ISAAC does not have a half wavelength plate, the better choice of cumulative angles would have been 0, 45, 45, 45, so as to achieve the same effects as in the FORS data (switching of the  $o$  and  $e$  images to minimize flat-field errors and Wollaston throughput uncertainties). These series of observations are repeated three times, resulting in complete sets *linK1*, *linK2* and *linK3*. Note that because of the rotation of the instrument, field stars are only visible in some of the rotation angles and rotate behind the mask at other angles. We note that a series of data were taken before *linK1* with an erroneous dithering pattern: the afterglow disappeared behind the aperture mask at the third and fourth angle. In further analysis we will only use the complete cycles *linK1*–*linK3*: the calibration as described below requires measurement of both  $q$  and  $u$  for a given parallactic angle.

### 2.2.2 Data reduction and calibration

Data were corrected for dark current, flat fielded and background subtracted using tasks in IRAF, and the four exposures of 60 s per angle per cycle were co-added. Aperture photometry was performed on the  $e$  and  $o$  images of the afterglow, in the same way as described above for FORS2. We compute the normalized Stokes parameters:

$$q = Q/I = \frac{(I_{o,0} - I_{e,0})}{(I_{o,0} + I_{e,0})} \quad \text{and} \quad u = U/I = \frac{(I_{o,45} - I_{e,45})}{(I_{o,45} + I_{e,45})},$$

using the data with rotation angles 0 and 45°. As we did not take data with 90° and 135° angles, we cannot use these to cancel out systematics as we did with the FORS2 data. We expect these effects to be of the same order or smaller as the statistical errors (the afterglow was faint in  $K$ ). We also compute Stokes parameters from the 22.5 and 67.5 data:

$$q_2 = (Q/I)_2 = \frac{(I_{o,22.5} - I_{e,22.5})}{(I_{o,22.5} + I_{e,22.5})} \quad \text{and} \\ u_2 = (U/I)_2 = \frac{(I_{o,67.5} - I_{e,67.5})}{(I_{o,67.5} + I_{e,67.5})},$$

which we will calibrate independently [they differ from  $(q, u)$  by a rotation in coordinate basis].

ISAAC is a Nasmyth focus instrument, and as such less well suited to accurate polarimetry: the instrumental polarization of Nasmyth instruments is dominated by reflection of the tertiary mirror M3 (at 45°, therefore introducing strong polarization which is highly

dependent on position or parallactic angle), which requires particular care in calibration. Our calibration strategy closely follows the recommendations of Joos et al. (2008) and Witzel et al. (2011). These authors highlight in their papers the great benefits of using a train of Mueller matrices to create a polarimetric model of the instrument plus telescope for Nasmyth mounted instruments: all elements contributing to instrumental polarization effects are described in  $4 \times 4$  matrices acting on the Stokes vector  $\mathbf{S}$ . These matrices are then multiplied to give a Mueller matrix of the whole telescope/instrument for a given wavelength and a given set-up. We refer to Joos et al. (2008) for a detailed breakdown of the required matrix components. The Mueller matrix  $\mathbf{M}(\theta, \lambda)$  describing the effects of the M3 mirror on the polarization is a function of the light incident angle  $\theta$ , wavelength  $\lambda$  and the refraction index components  $n$  and  $k$  of the reflecting surface of M3. For these latter values we use the values at the  $K$  band as derived by Witzel et al. (2011).

We obtained observations of the unpolarized DA white dwarf GJ 915 (WD 2359–434; Fossati et al. 2007) using the same instrument rotation angles as the science data and at a similar parallactic angle (60° at mid of the observation versus 50° for the mid of the range of the science series). Our calibrator observations were obtained just before the ISAAC science observations. We add to these observations from the European Southern Observatory (ESO) data archive of unpolarized white dwarf WD 1620–391 (using identical rotator angles as our data), taken on 2009 September 16, with parallactic angle 76°. Using these stars and the Mueller matrices described above we calibrate our Stokes parameters. Using our own standard star observations and those of 2008 gave consistent results within the errors. Because of the way we dithered our data and the low number of bright field stars, we cannot refine our calibration using field stars. We then rotate the  $(q_2, u_2)$  values to the same orientation as  $(q, u)$ . Because the source was fairly faint in the  $Ks$  band, the errors on the Stokes parameters of *linK1*–*3* are large, and we therefore combine them together, finding a combined  $q = 0.0204 \pm 0.0078$  and  $u = 0.00081 \pm 0.0083$ .

There are no field stars available for an independent GIP calibration in the  $Ks$  band, but we can estimate the likely contribution of GIP to the observed values by using the approximate relation  $p(\lambda) \propto \lambda^{-1.8}$  (see Martin & Whittet 1990). While the value of the exponent has fairly large uncertainty, it is clear that a GIP in the  $R$  band of ~0.45 per cent corresponds to an expected GIP contribution in the  $Ks$  band of <0.1 per cent, i.e. an order of magnitude smaller than the statistical uncertainties in the value above. We therefore make no correction to the  $Ks$ -band Stokes parameters above. Using the same techniques as for the FORS2 data we compute a bias-corrected linear polarization in the  $Ks$  band of  $2.0 \pm 0.8$  per cent with a position angle of  $10.9 \pm 20.9$ .

### 2.3 X-shooter spectroscopy

After the discovery of an optical afterglow, we activated our VLT X-shooter (mounted on UT2 of the VLT, Kueyen) programme for GRB afterglow spectroscopy (programme ID 084.A-0260, PI: Fynbo). We obtained  $4 \times 600$  s exposures with midpoint 0.1485 d ( $1.283 \times 10^4$  s) after burst. X-shooter is an echelle spectrograph with three arms, the UVB, VIS and NIR arms, separated by dichroics, resulting in a wavelength coverage ~0.3–2.4  $\mu\text{m}$ . We used a  $1 \times 2$  binning in the UVB and VIS arms (binning in the wavelength coordinate). A 5 arcsec nod throw was used to facilitate accurate sky subtraction, particularly important in the NIR arm, resulting in exposures taken in an ABBA pattern. We processed the data using

version 1.3.0 of the ESO X-shooter data reduction pipeline (Goldoni et al. 2006), using the so-called physical mode.

Flux calibration is achieved using exposures of the flux standard star BD+17 4708. Telluric line correction of the NIR arm spectrum was performed using methods outlined in Wiersema (2011) with the SPECTOOL software (Cushing, Vacca & Rayner 2004), using observations of the B9V star HD 16226. The resulting spectra are normalized.

## 2.4 Optical and near-infrared photometry

### 2.4.1 GROND afterglow photometry

The seven-channel Gamma-Ray Burst Optical and Near-Infrared Detector (GROND; Greiner et al. 2008) mounted on the ESO 2.2 m telescope observed the field of GRB 091018 using the  $g'$ ,  $r'$ ,  $i'$ ,  $z'$ ,  $J$ ,  $H$ ,  $Ks$  filters beginning as soon as the source became visible from La Silla observatory (Filgas et al. 2009). Photometric calibration was achieved through observations of photometric standard star fields. A spectral energy distribution using some of the GROND data presented here was published earlier in Greiner et al. (2011).

### 2.4.2 Faulkes Telescope South afterglow photometry

We observed the optical afterglow using the Faulkes Telescope South (FTS), at Siding Spring, Australia. Observations were performed at two different epochs (about 15.3 h and 3.7 d after the burst event), using the  $R$  and  $i$  filters. These observations are complementary to those of GROND, filling the gap in coverage during daytime in Chile. All the images were cross-calibrated using the GROND field star measurement.

### 2.4.3 VLT afterglow photometry

As part of our linear and circular polarization monitoring campaign described above, a large series of acquisition images were taken for accurate positioning of the afterglow within the aperture mask. Within each of these images the afterglow is detected at good signal-to-noise levels. We reduce the 14 FORS2 and two ISAAC acquisition images using flat fields, dark and bias fields taken the same night. The FORS2 acquisition data were taken using the  $R_{\text{special}}$  filter, and the ISAAC data using the  $Ks$  filter. We use a sample of field stars in the GROND data to bring the FORS2 acquisition photometry to the same homogeneous calibration. The ISAAC data were calibrated using four 2MASS stars in the field of view. The resulting magnitudes were converted to  $AB$  magnitudes; the resulting values are reported in Table 3.

In addition to the polarimetry acquisition images, we also photometer the acquisition image taken for the X-shooter spectroscopy, calibrating on to the GROND system.

### 2.4.4 Gemini-South afterglow and host photometry

We followed the late-time afterglow with Gemini Multi-Object Spectrograph (GMOS)-South, mounted on the Gemini South telescope, Chile. We observed the source at three epochs, in Sloan  $r$  band (GMOS filter  $r\_G0326$ ), see Table 3. We reduce the GMOS images using twilight flat fields and bias fields taken the same night using tasks from the GEMINI packages in IRAF. In all three data sets the host galaxy of the burst is visible. Photometric calibration is performed relative to the GROND calibration.

**Table 3.** Log of our photometry. All magnitudes are  $AB$  magnitudes. These magnitudes are not corrected for the Galactic foreground extinction.

Instrument, Filter	Time since burst (d)	Exposure time (s)	Magnitude
GROND, $g$	0.126 93	115	19.06 $\pm$ 0.04
	0.129 06	115	19.05 $\pm$ 0.03
	0.131 25	115	19.08 $\pm$ 0.02
	0.133 44	115	19.06 $\pm$ 0.02
	0.135 75	115	19.06 $\pm$ 0.02
	0.137 93	115	19.07 $\pm$ 0.02
	0.140 12	115	19.08 $\pm$ 0.01
	0.142 31	115	19.09 $\pm$ 0.01
	0.144 57	115	19.11 $\pm$ 0.02
	0.146 70	115	19.12 $\pm$ 0.02
	0.148 89	115	19.14 $\pm$ 0.02
	0.151 09	115	19.12 $\pm$ 0.02
	0.153 30	115	19.15 $\pm$ 0.02
	0.155 51	115	19.15 $\pm$ 0.02
	0.157 62	115	19.14 $\pm$ 0.02
	0.159 85	115	19.15 $\pm$ 0.02
	0.162 16	115	19.16 $\pm$ 0.02
	0.164 29	115	19.17 $\pm$ 0.02
	0.166 48	115	19.17 $\pm$ 0.02
	0.168 67	115	19.16 $\pm$ 0.02
	0.170 96	115	19.17 $\pm$ 0.02
	0.173 18	115	19.22 $\pm$ 0.02
	0.175 41	115	19.23 $\pm$ 0.02
	0.177 65	115	19.26 $\pm$ 0.02
	0.179 98	115	19.32 $\pm$ 0.02
	0.182 14	115	19.33 $\pm$ 0.02
	0.184 37	115	19.34 $\pm$ 0.02
	0.186 60	115	19.34 $\pm$ 0.02
	0.188 91	115	19.35 $\pm$ 0.02
	0.191 15	115	19.34 $\pm$ 0.02
	0.193 33	115	19.36 $\pm$ 0.02
	0.195 52	115	19.38 $\pm$ 0.02
	0.197 81	115	19.39 $\pm$ 0.02
0.199 96	115	19.42 $\pm$ 0.02	
0.202 14	115	19.46 $\pm$ 0.02	
0.204 33	115	19.47 $\pm$ 0.02	
0.206 67	115	19.48 $\pm$ 0.02	
0.208 86	115	19.48 $\pm$ 0.02	
0.211 05	115	19.51 $\pm$ 0.02	
0.213 24	115	19.54 $\pm$ 0.02	
0.215 56	115	19.54 $\pm$ 0.02	
0.217 67	115	19.53 $\pm$ 0.02	
0.219 85	115	19.54 $\pm$ 0.02	
0.222 04	115	19.54 $\pm$ 0.02	
0.224 33	115	19.53 $\pm$ 0.02	
0.226 48	115	19.51 $\pm$ 0.02	
0.228 67	115	19.52 $\pm$ 0.02	
0.230 86	115	19.54 $\pm$ 0.02	
0.233 13	115	19.54 $\pm$ 0.02	
0.235 26	115	19.54 $\pm$ 0.02	
0.237 49	115	19.54 $\pm$ 0.02	
0.239 77	115	19.54 $\pm$ 0.02	
0.348 60	675	20.01 $\pm$ 0.02	
0.448 72	688	20.21 $\pm$ 0.02	
1.209 17	675	21.76 $\pm$ 0.04	
1.309 36	688	21.82 $\pm$ 0.04	
1.494 85	688	22.02 $\pm$ 0.05	
2.226 73	1727	22.53 $\pm$ 0.04	
3.157 88	1722	22.94 $\pm$ 0.07	
GROND, $r$	0.126 93	115	18.87 $\pm$ 0.03
	0.129 06	115	18.86 $\pm$ 0.02

**Table 3** – *continued*

Instrument, Filter	Time since burst (d)	Exposure time (s)	Magnitude
	0.131 25	115	18.85 ± 0.02
	0.133 44	115	18.87 ± 0.02
	0.135 75	115	18.88 ± 0.02
	0.137 93	115	18.91 ± 0.02
	0.140 12	115	18.91 ± 0.02
	0.142 31	115	18.92 ± 0.02
	0.144 57	115	18.93 ± 0.02
	0.146 70	115	18.93 ± 0.02
	0.148 89	115	18.94 ± 0.02
	0.151 09	115	18.94 ± 0.02
	0.153 30	115	18.94 ± 0.02
	0.155 51	115	18.96 ± 0.02
	0.157 62	115	18.97 ± 0.02
	0.159 85	115	18.98 ± 0.02
	0.162 16	115	18.98 ± 0.02
	0.164 29	115	18.99 ± 0.02
	0.166 48	115	18.98 ± 0.02
	0.168 67	115	18.97 ± 0.02
	0.170 96	115	18.99 ± 0.02
	0.173 18	115	19.03 ± 0.02
	0.175 41	115	19.06 ± 0.02
	0.177 65	115	19.08 ± 0.02
	0.179 98	115	19.11 ± 0.02
	0.182 14	115	19.14 ± 0.02
	0.184 37	115	19.15 ± 0.02
	0.186 60	115	19.17 ± 0.02
	0.188 91	115	19.15 ± 0.02
	0.191 15	115	19.17 ± 0.02
	0.193 33	115	19.17 ± 0.02
	0.195 52	115	19.18 ± 0.02
	0.197 81	115	19.21 ± 0.02
	0.199 96	115	19.24 ± 0.02
	0.202 14	115	19.25 ± 0.02
	0.204 33	115	19.27 ± 0.02
	0.206 67	115	19.30 ± 0.02
	0.208 86	115	19.32 ± 0.02
	0.211 05	115	19.33 ± 0.02
	0.213 24	115	19.33 ± 0.02
	0.215 56	115	19.37 ± 0.02
	0.217 67	115	19.36 ± 0.02
	0.219 85	115	19.37 ± 0.02
	0.222 04	115	19.36 ± 0.02
	0.224 33	115	19.33 ± 0.02
	0.226 48	115	19.34 ± 0.02
	0.228 67	115	19.35 ± 0.02
	0.230 86	115	19.35 ± 0.02
	0.233 13	115	19.34 ± 0.02
	0.235 26	115	19.35 ± 0.02
	0.237 49	115	19.35 ± 0.02
	0.239 77	115	19.37 ± 0.02
	0.348 60	675	19.82 ± 0.02
	0.448 72	688	20.01 ± 0.02
	1.209 17	675	21.59 ± 0.03
	1.309 36	688	21.68 ± 0.03
	1.494 85	688	21.88 ± 0.05
	2.226 73	1727	22.34 ± 0.04
	3.157 88	1722	22.81 ± 0.10
GROND, <i>i</i>	0.126 93	115	18.71 ± 0.04
	0.129 06	115	18.71 ± 0.03
	0.131 25	115	18.72 ± 0.02
	0.133 44	115	18.75 ± 0.03
	0.135 75	115	18.76 ± 0.03

**Table 3** – *continued*

Instrument, Filter	Time since burst (d)	Exposure time (s)	Magnitude
	0.137 93	115	18.79 ± 0.02
	0.140 12	115	18.79 ± 0.02
	0.142 31	115	18.78 ± 0.02
	0.144 57	115	18.81 ± 0.03
	0.146 70	115	18.80 ± 0.02
	0.148 89	115	18.82 ± 0.02
	0.151 09	115	18.80 ± 0.02
	0.153 30	115	18.84 ± 0.03
	0.155 51	115	18.84 ± 0.02
	0.157 62	115	18.84 ± 0.02
	0.159 85	115	18.84 ± 0.02
	0.162 16	115	18.85 ± 0.02
	0.164 29	115	18.84 ± 0.02
	0.166 48	115	18.84 ± 0.02
	0.168 67	115	18.82 ± 0.02
	0.170 96	115	18.84 ± 0.02
	0.173 18	115	18.88 ± 0.02
	0.175 41	115	18.91 ± 0.02
	0.177 65	115	18.95 ± 0.02
	0.179 98	115	18.97 ± 0.02
	0.182 14	115	19.01 ± 0.02
	0.184 37	115	19.03 ± 0.02
	0.186 60	115	19.02 ± 0.02
	0.188 91	115	19.03 ± 0.02
	0.191 15	115	19.02 ± 0.02
	0.193 33	115	19.02 ± 0.02
	0.195 52	115	19.02 ± 0.02
	0.197 81	115	19.07 ± 0.02
	0.199 96	115	19.09 ± 0.02
	0.202 14	115	19.12 ± 0.02
	0.204 33	115	19.13 ± 0.02
	0.206 67	115	19.15 ± 0.02
	0.208 86	115	19.15 ± 0.02
	0.211 05	115	19.16 ± 0.02
	0.213 24	115	19.18 ± 0.02
	0.215 56	115	19.20 ± 0.02
	0.217 67	115	19.21 ± 0.02
	0.219 85	115	19.21 ± 0.02
	0.222 04	115	19.18 ± 0.02
	0.224 33	115	19.21 ± 0.02
	0.226 48	115	19.20 ± 0.02
	0.228 67	115	19.21 ± 0.02
	0.230 86	115	19.21 ± 0.02
	0.233 13	115	19.24 ± 0.03
	0.235 26	115	19.23 ± 0.02
	0.237 49	115	19.21 ± 0.03
	0.239 77	115	19.21 ± 0.03
	0.348 60	675	19.67 ± 0.02
	0.448 72	688	19.85 ± 0.02
	1.209 17	675	21.47 ± 0.06
	1.309 36	688	21.51 ± 0.06
	1.494 85	688	21.64 ± 0.10
	2.226 73	1727	22.03 ± 0.08
	3.157 88	1722	22.53 ± 0.13
GROND, <i>z</i>	0.126 93	115	18.59 ± 0.05
	0.129 06	115	18.58 ± 0.05
	0.131 25	115	18.58 ± 0.03
	0.133 44	115	18.59 ± 0.03
	0.135 75	115	18.61 ± 0.03
	0.137 93	115	18.65 ± 0.03
	0.140 12	115	18.63 ± 0.03
	0.142 31	115	18.65 ± 0.03

Table 3 – continued

Instrument, Filter	Time since burst (d)	Exposure time (s)	Magnitude
	0.144 57	115	18.64 ± 0.03
	0.146 70	115	18.66 ± 0.03
	0.148 89	115	18.70 ± 0.03
	0.151 09	115	18.71 ± 0.03
	0.153 30	115	18.70 ± 0.03
	0.155 51	115	18.68 ± 0.03
	0.157 62	115	18.71 ± 0.03
	0.159 85	115	18.71 ± 0.03
	0.162 16	115	18.68 ± 0.03
	0.164 29	115	18.67 ± 0.03
	0.166 48	115	18.69 ± 0.03
	0.168 67	115	18.68 ± 0.03
	0.170 96	115	18.70 ± 0.03
	0.173 18	115	18.74 ± 0.03
	0.175 41	115	18.80 ± 0.03
	0.177 65	115	18.82 ± 0.03
	0.179 98	115	18.82 ± 0.03
	0.182 14	115	18.87 ± 0.03
	0.184 37	115	18.90 ± 0.03
	0.186 60	115	18.87 ± 0.03
	0.188 91	115	18.89 ± 0.03
	0.191 15	115	18.88 ± 0.03
	0.193 33	115	18.88 ± 0.03
	0.195 52	115	18.89 ± 0.02
	0.197 81	115	18.90 ± 0.03
	0.199 96	115	18.91 ± 0.03
	0.202 14	115	18.94 ± 0.03
	0.204 33	115	18.93 ± 0.03
	0.206 67	115	18.99 ± 0.03
	0.208 86	115	19.03 ± 0.03
	0.211 05	115	19.04 ± 0.03
	0.213 24	115	19.01 ± 0.03
	0.215 56	115	19.06 ± 0.03
	0.217 67	115	19.05 ± 0.03
	0.219 85	115	19.08 ± 0.03
	0.222 04	115	19.09 ± 0.03
	0.224 33	115	19.07 ± 0.03
	0.226 48	115	19.08 ± 0.03
	0.228 67	115	19.10 ± 0.03
	0.230 86	115	19.12 ± 0.03
	0.233 13	115	19.06 ± 0.03
	0.235 26	115	19.05 ± 0.03
	0.237 49	115	19.07 ± 0.03
	0.239 77	115	19.07 ± 0.03
	0.348 60	675	19.51 ± 0.02
	0.448 72	688	19.70 ± 0.03
	1.209 17	675	21.24 ± 0.07
	1.309 36	688	21.32 ± 0.08
	1.494 85	688	21.61 ± 0.12
	2.226 73	1727	22.00 ± 0.09
	3.157 88	1722	22.64 ± 0.20
GROND, J	0.130 48	730	18.34 ± 0.03
	0.139 32	730	18.38 ± 0.03
	0.148 12	730	18.40 ± 0.03
	0.156 88	730	18.45 ± 0.03
	0.165 70	730	18.38 ± 0.03
	0.174 60	730	18.52 ± 0.03
	0.183 59	730	18.58 ± 0.03
	0.192 51	730	18.58 ± 0.03
	0.201 36	730	18.68 ± 0.03
	0.210 24	735	18.73 ± 0.03
	0.219 09	727	18.82 ± 0.03

Table 3 – continued

Instrument, Filter	Time since burst (d)	Exposure time (s)	Magnitude
	0.227 89	730	18.77 ± 0.03
	0.236 74	730	18.79 ± 0.03
	0.348 89	730	19.17 ± 0.03
	0.449 03	730	19.37 ± 0.04
GROND, H	0.130 48	730.08	18.19 ± 0.05
	0.139 32	730.08	18.18 ± 0.04
	0.148 12	730.08	18.24 ± 0.04
	0.156 88	730.08	18.27 ± 0.03
	0.165 70	730.08	18.22 ± 0.04
	0.174 60	730.08	18.31 ± 0.03
	0.183 59	730.08	18.34 ± 0.03
	0.192 51	730.08	18.38 ± 0.03
	0.201 36	730.08	18.51 ± 0.03
	0.210 24	734.62	18.53 ± 0.04
	0.219 09	726.82	18.60 ± 0.04
	0.227 89	730.08	18.55 ± 0.04
	0.236 74	730.08	18.57 ± 0.03
	0.348 89	730.08	19.04 ± 0.09
	0.449 03	730.08	19.22 ± 0.09
GROND, K	0.130 48	730	17.95 ± 0.07
	0.139 32	730	18.06 ± 0.07
	0.148 12	730	17.96 ± 0.06
	0.156 88	730	18.10 ± 0.06
	0.165 70	730	18.08 ± 0.06
	0.174 60	730	18.17 ± 0.06
	0.183 59	730	18.25 ± 0.06
	0.192 51	730	18.21 ± 0.06
	0.201 36	730	18.37 ± 0.06
	0.210 24	735	18.32 ± 0.06
	0.219 09	727	18.35 ± 0.06
	0.227 89	730	18.32 ± 0.06
	0.236 74	730	18.42 ± 0.06
	0.348 89	730	18.83 ± 0.07
	0.449 03	730	19.07 ± 0.08
FORS2, $R_{\text{special}}^a$	0.123 84	20	18.85 ± 0.03
	0.137 07	20	18.90 ± 0.03
	0.172 57	30	19.03 ± 0.03
	0.187 47	30	19.16 ± 0.03
	0.220 93	30	19.36 ± 0.03
	0.254 26	30	19.37 ± 0.03
	0.444 61	30	20.01 ± 0.03
	1.129 10	60	21.33 ± 0.04
	1.163 63	60	21.43 ± 0.03
	1.197 48	60	21.46 ± 0.03
	1.343 18	60	21.45 ± 0.03
	1.375 20	60	21.56 ± 0.03
	1.432 64	60	21.71 ± 0.03
	2.369 48	120	22.40 ± 0.05
X-shooter, $R^a$	0.131 725	20	18.91 ± 0.02
ISAAC, $K_s$	0.215 72	60	18.70 ± 0.10
	0.273 02	60	19.01 ± 0.09
Gemini GMOS, $r$	6.269 22	900	23.25 ± 0.04
	21.280 34	900	23.42 ± 0.05
	23.392 84	720	23.40 ± 0.10
FT-S, Bessel $R^a$	0.662 38	1800	20.82 ± 0.02
	0.758 56	1800	20.99 ± 0.03
	0.823 98	1800	21.23 ± 0.03
	3.717 35	3600	23.03 ± 0.09

Table 3 – *continued*

Instrument, Filter	Time since burst (d)	Exposure time (s)	Magnitude
FT-S, Sloan <i>i</i>	0.639 24	1800	20.49 ± 0.02
	0.735 42	1800	20.71 ± 0.03
	0.800 83	1800	20.79 ± 0.05
	0.880 65	1800	20.96 ± 0.04
	3.771 79	900	22.38 ± 0.42
	3.783 00	900	22.42 ± 0.35
UVOT, <i>white</i>	0.0017	149.8	15.33 ± 0.02
	0.0066	19.8	16.70 ± 0.05
	0.0086	19.7	16.97 ± 0.05
	0.0108	149.7	17.24 ± 0.03
	0.0136	19.8	17.45 ± 0.06
	0.0693	199.8	19.07 ± 0.04
	0.1471	361	19.75 ± 0.05
	0.3406	1614.2	20.59 ± 0.07
	1.0156	566.6	21.73 ± 0.18
	1.4510	40 789.7	22.66 ± 0.27
	1.9175	29 362	22.86 ± 0.19
	2.5761	29 994.8	23.35 ± 0.28
	3.2865	46 836	22.82 ± 0.18
	3.9556	58 829.1	22.64 ± 0.25
	5.2311	138 900.4	23.79 ± 0.36
6.6682	98 684.1	23.26 ± 0.23	
8.4084	121 624.7	>23.81	
UVOT, <i>v</i>	0.0072	19.8	16.34 ± 0.14
	0.0092	19.8	16.84 ± 0.18
	0.0132	194.1	16.92 ± 0.14
	0.0740	199.8	18.51 ± 0.17
	0.2803	476	19.45 ± 0.23
	0.7414	36 383.3	20.63 ± 0.26
UVOT, <i>b</i>	0.0063	19.7	16.20 ± 0.08
	0.0083	19.7	16.45 ± 0.09
	0.0143	191.8	17.22 ± 0.09
	0.1304	1911.2	19.38 ± 0.14
	0.1432	299.8	19.19 ± 0.12
	0.3259	906.9	20.15 ± 0.15
	0.4128	686.9	20.15 ± 0.17
	0.6129	790.9	20.27 ± 0.18
	0.9072	16 951.2	21.24 ± 0.34
	1.0088	603.3	20.75 ± 0.3
UVOT, <i>u</i>	0.0047	249.7	16.05 ± 0.03
	0.0080	19.7	16.71 ± 0.08
	0.0140	193.5	17.27 ± 0.08
	0.0811	199.7	19.00 ± 0.08
	0.2119	717.9	19.89 ± 0.08
	0.4035	907	20.57 ± 0.11
	0.4797	693	20.56 ± 0.13
	0.6411	7484.4	21.24 ± 0.14
	0.8418	7481.9	22.23 ± 0.35
	1.5784	63 376.6	22.69 ± 0.32
	2.2041	34 276.6	22.35 ± 0.35
	2.9722	87 931	22.96 ± 0.3
	3.6073	12 000.2	22.40 ± 0.32
5.0600	132 684.3	23.01 ± 0.35	
7.4991	278 015.6	23.33 ± 0.28	
UVOT, <i>uvw1</i>	0.0077	19.8	17.41 ± 0.13
	0.0098	19.8	17.70 ± 0.15
	0.0137	193.7	17.83 ± 0.11
	0.0788	199.7	19.80 ± 0.13
	0.1885	434.9	20.27 ± 0.12
	0.3930	899.7	20.96 ± 0.13
	0.4704	899.8	21.35 ± 0.17

Table 3 – *continued*

Instrument, Filter	Time since burst (d)	Exposure time (s)	Magnitude
	0.6312	7587.9	22.01 ± 0.19
	0.9308	24 671.6	22.34 ± 0.24
UVOT, <i>uvm2</i>	0.0095	19.8	17.66 ± 0.17
	0.0124	19.7	18.05 ± 0.21
	0.0764	199.8	20.02 ± 0.17
	0.4599	899.8	21.29 ± 0.17
	0.5460	790.2	21.70 ± 0.23
	0.7027	8389.3	22.10 ± 0.21
	0.8646	899.7	22.04 ± 0.28
UVOT, <i>uvw2</i>	0.0069	19.8	17.88 ± 0.15
	0.0089	19.8	18.05 ± 0.16
	0.0139	19.8	18.52 ± 0.20
	0.0717	199.7	20.37 ± 0.16
	0.2581	748.1	21.27 ± 0.14
	0.5256	899.8	21.81 ± 0.18
	0.8314	19 056.1	23.05 ± 0.32
	1.8138	102 925.1	>21.90
	3.5897	191 453.2	>22.51
	7.1639	325 158.9	>22.50

<sup>a</sup>Calibrated on to Sloan *r* using GROND.

#### 2.4.5 UVOT afterglow photometry

*Swift*'s UVOT (Roming et al. 2005) began settled observations 68 s after the BAT trigger, beginning with a 150 s exposure in the white filter followed by a 245 s exposure in the *u* band and thereafter cycling through all seven lenticular filters. We performed photometry and created light curves using the tool *uvotproduct* provided in the *Swift* software. The latest calibration data as of 2011 July were used. We binned the data requiring a minimum detection significance of  $3\sigma$  per bin; errors are given at the  $1\sigma$  level.

## 3 RESULTS

### 3.1 Light curves and spectral energy distributions

#### 3.1.1 X-ray light curve fits

The *Swift* XRT X-ray data, as analysed through the *Swift* XRT catalogue<sup>3</sup> (see Evans et al. 2009 for details), show an initial shallow decay phase, with power-law decay index  $\alpha_1 = 0.41_{-0.08}^{+0.06}$ . A break in the light curve at  $587_{-91}^{+85}$  s sees the decay continue with a steeper index  $\alpha_2 = 1.24 \pm 0.04$ . Between  $\sim 10^4$  and  $10^5$  s a broad bump is visible in the X-ray light curve. The *Swift* XRT catalogue lists the best-fitting solution ( $\chi^2/\text{dof} = 117/133$ ) using two breaks in quick succession, at  $2.24_{-0.62}^{+0.39} \times 10^4$  and  $2.69_{-0.16}^{+1.29} \times 10^4$  s, with the first leading to a negative index (i.e. a brightening, but with poorly constrained index) and the last break leading to a final decay index of  $\alpha_4 = 1.59_{-0.11}^{+0.12}$ . It is likely that the behaviour between  $\sim 10^4$  and  $10^5$  s is the result of a system of late-time flares (or some other form of short time-scale rebrightening), in which case a more realistic alternative description may be that of a single break at  $4.7_{-1.0}^{+2.6} \times 10^4$  s, with  $\alpha_2 = 1.17 \pm 0.03$  and  $\alpha_3 = 1.54_{-0.13}^{+0.18}$ . This gives a poorer  $\chi^2$  statistic ( $\chi^2/\text{dof} = 137/135$ ), as a cluster of data points interpreted as due to flaring/bump in this scenario are off the best fit. The X-ray light curve and the fit are shown in Fig. 10.

<sup>3</sup> [http://www.swift.ac.uk/xrt\\_live\\_cat/](http://www.swift.ac.uk/xrt_live_cat/)

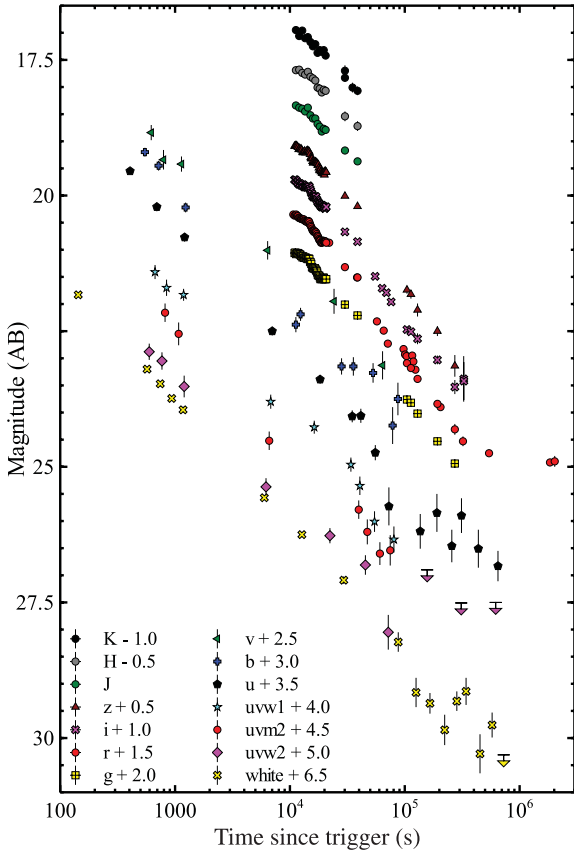


**Figure 4.** Optical light curves used in this paper (for their values, see Table 3). All magnitudes are in the AB photometric system, and the FORS2  $R_{\text{Special}}$  magnitudes are converted to  $r$ . Light curves in different bands are offset for clarity.

### 3.1.2 Optical light curve fits

The optical light curves presented in this paper have their densest coverage through the GROND observations, as described above. Figs 4, 5, 6 and 7 show the presence of bumps in the light curve, on top of the usual power-law decay. Bumps in afterglow light curves are fairly common, though they require good signal to noise to be identified. Three distinct bumps, each lasting roughly half an hour, are readily visible in the first night data, and are indicated by dashed vertical lines in Fig. 6 (see Section 3.1; these bumps are also detected by PROMPT (Panchromatic Robotic Optical Monitoring and Polarimetry Telescopes), LaCluyze et al. 2009). Similar to the X-rays, the presence of bumps makes the light curve fits somewhat complex:  $\chi^2$  fit statistics are largely driven by data points belonging to bumps covered by GROND. To find a best possible way to discern bumps and power-law breaks, we use the method described in Curran et al. (2007b): data from all filters were combined through a free offset fit (i.e. we assume that data from all filters have the same temporal decay but we make no assumptions regarding the relative offsets). Simulated annealing is used to fit the offsets, temporal indices and break times, and a Monte Carlo analysis with synthetic data sets is used for error determination: the normalization error is added in quadrature to the data points in the resulting combined light curve. We exclude very early data (i.e. the first UVOT data point at around 100 s), late-time UVOT data ( $>10^5$  s) and the late-time Gemini data, which are nearly entirely host dominated. The resulting shifted data points are placed on an arbitrarily scaled flux scale, and we fit this resulting dense light curve. We fit a broken power

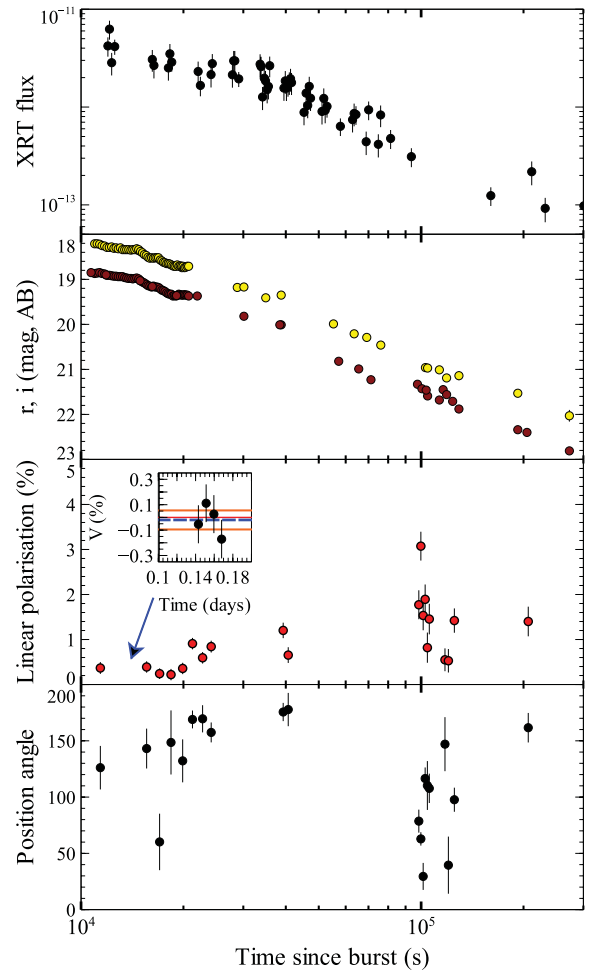


**Figure 5.** The linear polarimetry light curve with broad-band light curves as reference. The top panel shows the XRT X-ray light curve over this interval. The panel below that shows the  $r$  (red) and  $i$  (yellow) light curves over this time interval ( $i$  magnitudes shifted by  $-0.5$  mag). The lower two panels show the linear polarization and polarization position angle. We plot the polarimetric data points as observed, i.e. before correction for Galactic dust-induced polarization. The inset shows the circular polarimetry (four measurements of Stokes  $V/I$ ) performed in between  $lin1$  and  $lin2$ . The horizontal thin red line shows the  $V/I = 0$  level, and the blue dashed line shows the average of the four data points,  $V/I = -0.0002$ , with the solid orange lines indicating the error  $0.00075$ , leading to a  $2\sigma$  limit 0.15 per cent.

law, which gives a reduced  $\chi^2 = 1.68$  for 365 degrees of freedom (dof). We then add Gaussian functions one by one to empirically take care of the bumps in the light curve (i.e. this is not a physically motivated description of light curve bumps). The best fit is obtained using three Gaussians and a broken power law, and is displayed in Fig. 10, with reduced  $\chi^2 = 1.12$  (356 dof). We find best fitting parameters for the broken power-law component of  $\alpha_1 = 0.81 \pm 0.01$ ,  $\alpha_2 = 1.33 \pm 0.02$  and a break time of  $t_{\text{break}} = 3.23 \pm 0.16 \times 10^4$  s. The three Gaussians have best fitting centre times  $1.43 \pm 0.01 \times 10^4$ ,  $1.68 \pm 0.01 \times 10^4$  and  $2.13 \pm 0.06 \times 10^4$  s. Their widths as given by the standard deviation of the fitted Gaussians are  $\sigma = 1140 \pm 200$ ,  $370 \pm 80$  and  $1026 \pm 230$  s, respectively, though we note that the third bump is only partially covered by data points, resulting in the larger errors in central time and width. Adding the late-time Gemini data to the data set after subtracting the host brightness (the last Gemini epoch) does not change the fits.

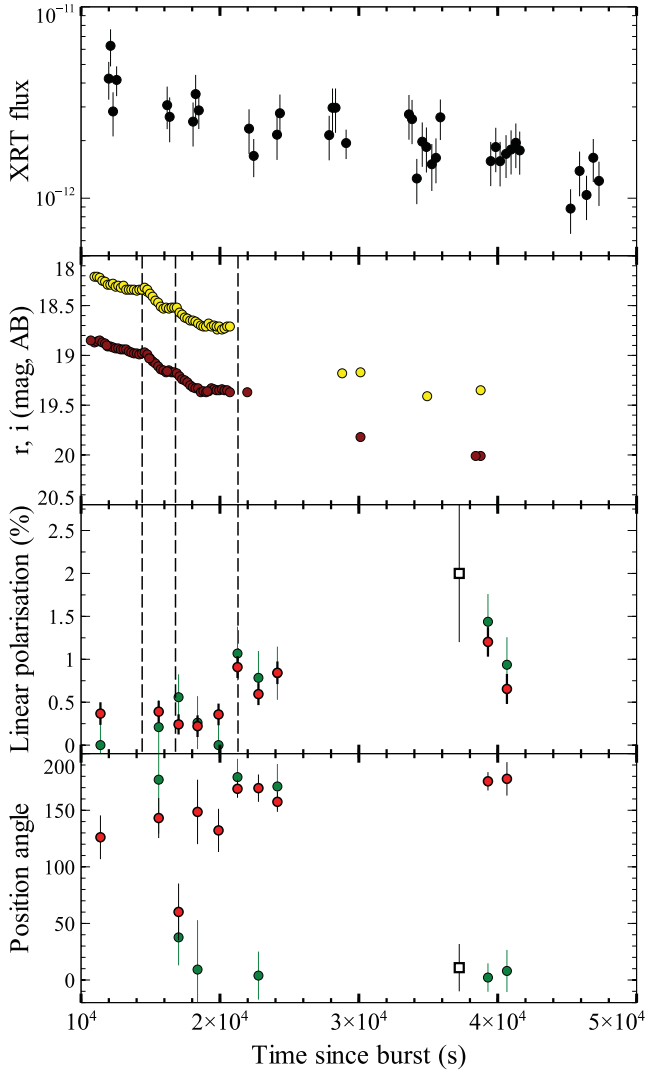


**Figure 6.** Panels are as in Fig. 5, showing the behaviour of the source during the first night of polarimetric observations (*lin1–lin10*) – note the linear time axis. The lower two panels show the linear polarization and polarization position angle, but this time we plot both the polarimetric data points as observed (red) and after correction for Galactic dust-induced polarization (green). The open black squares give the ISAAC *Ks*-band polarization degree and angle. Data points with zero GIP-corrected polarization have no associated position angle measurement. We note that position angles range  $[0–180]$ , i.e. one can add  $180^\circ$  to green data points with low angle values (to any data point one can add or subtract  $180^\circ$ ) to visually verify that they behave similarly to the trend seen in the data before GIP correction. The dashed vertical lines indicate the centres of three bumps found in the optical light curve (fits are in Section 3.1).

### 3.1.3 Spectral energy distributions and light curve interpretation

In a study of the host galaxy dust extinction properties of sightlines towards GRB afterglows using single epoch broad-band spectral energy distributions (SEDs), Schady et al. (2012) report on a late-time SED of the afterglow of GRB 091018. This SED (at  $3 \times 10^4$  s, using GROND, UVOT and XRT data) is best fitted with a broken power law, indicating the presence of a synchrotron cooling break in between X-ray and optical/UV wavelengths. We extend this analysis, fitting the X-ray–optical SEDs at three representative epochs: at  $10^4$ ,  $3 \times 10^4$  and  $10^5$  s, using a fitting method described in detail

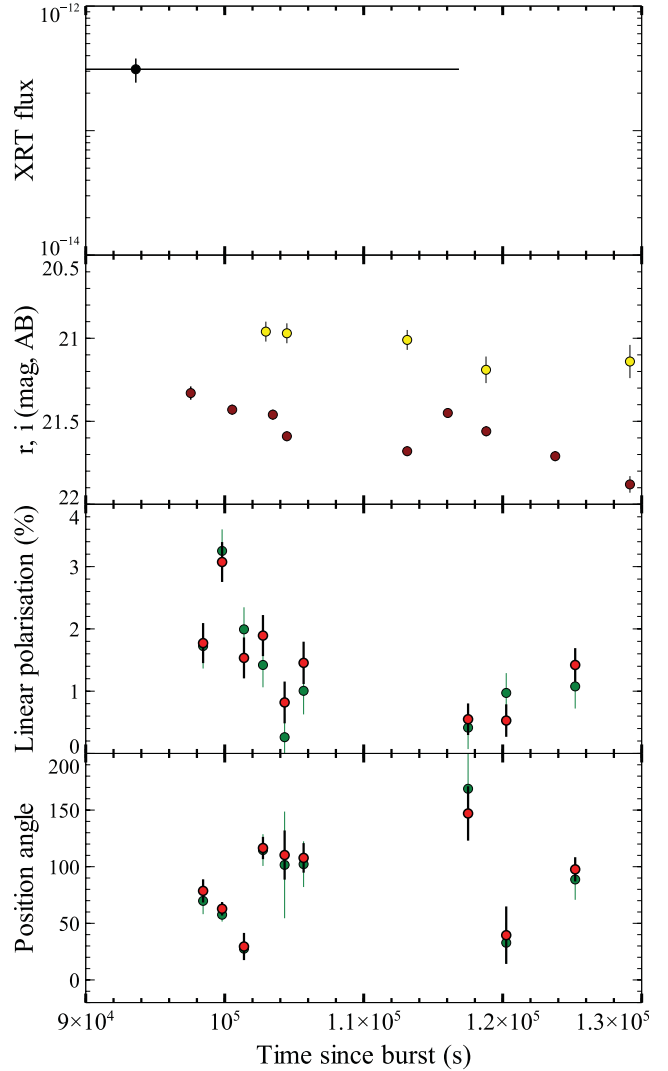


**Figure 7.** Panels are as in Fig. 5, this time showing the behaviour of the source during the second night of polarimetric observations (*lin11–lin19*). A  $180^\circ$  rotation of the position angle is apparent, sampled in the first six data points.

in Krühler et al. (2011). We assume that there is no change in X-ray absorption and optical extinction between the three epochs. We fit using a broken power law (with the two power-law indices linked with  $\beta_1 = \beta_2 - 0.5$ ) and Small Magellanic Cloud-like extinction law, shown by Schady et al. (2012) to be the best fit for this afterglow, with the  $E(B - V)$  and  $N(\text{H})$  fit simultaneously for all three epochs. Bands with a possible contribution from the Lyman limit are excluded from the fit. The fit statistics are computed using C statistics (C-stat) in the X-rays (see Evans et al. 2009) and  $\chi^2$  in the optical. The fits are displayed in Fig. 11. The three SEDs are best fitted ( $\chi^2 = 27.04$  using 31 bins, C-stat = 315.35 using 433 bins) with the following properties (errors at 90 per cent level confidence):  $E(B - V) = 0.024^{+0.005}_{-0.006}$ ,  $N(\text{H}) = 1.7 \pm 0.8 \times 10^{21} \text{ cm}^{-2}$  and power-law slope  $\beta_1 = 0.58 \pm 0.07$ . These values are in agreement with the results of Schady et al. (2012). We find power-law break energies  $E_{\text{break}} = 0.05^{+0.1}_{-0.03}$ ,  $0.05^{+0.1}_{-0.03}$  and  $0.025^{+0.05}_{-0.017}$  keV for the SEDs at 10, 30 and 100 ks, respectively.

We now compare the decay indices and spectral indices to closure relations for some simple models. The spectral indices found

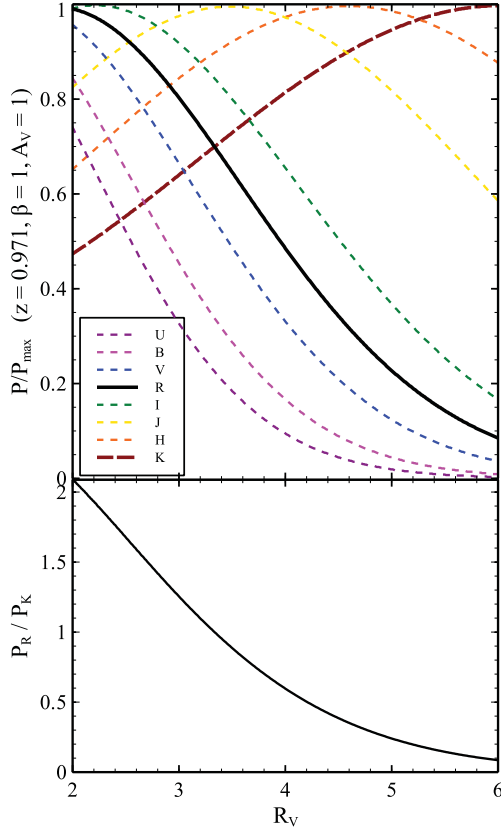


**Figure 8.** Upper panel:  $P/P_{\max}$  for a range of  $R_V$  values, at the redshift of GRB 091018 and using host galaxy extinction  $A_V = 1$  magnitude. Lower panel: resulting ratio of  $R$ -band and  $K$ -band linear polarization (in the case when all detected polarization is due to dust scattering in the host galaxy).

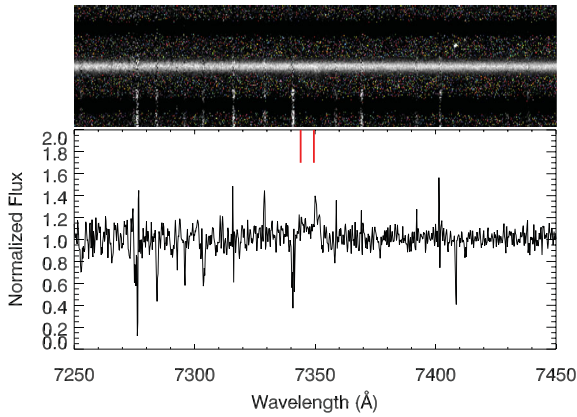


**Figure 9.** Emission lines of the [O II] doublet in the spectrum. The 2D spectrum is shown in the top panel. Weak residuals from imperfect subtraction of sky emission lines can be seen as vertical stripes, also showing up as narrow residuals in the 1D spectrum.

from the SED fits imply a power-law index for the electron energy distribution  $p = 2.16 \pm 0.14$ . If the blast wave propagates in a homogeneous density medium, the predicted afterglow decay index for the regime  $\nu < \nu_c$  is  $3(p-1)/4 = 0.87 \pm 0.11$ , and for  $\nu > \nu_c$  it is  $1.12 \pm 0.11$ . A wind-like medium (where density decreases with  $r^2$ ) for  $\nu < \nu_c$  would imply  $\alpha = (3p-2)/4 = 1.37 \pm 0.11$ , and

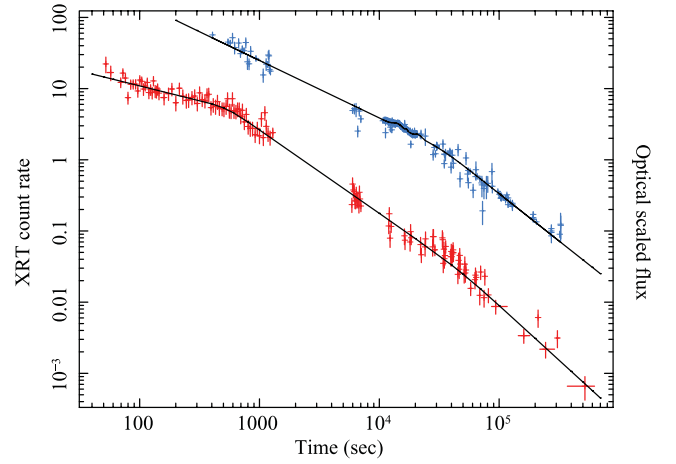


**Figure 10.** The optical light curve, in arbitrary flux units as described in Section 3.1, is shown in blue (top), with the best fitting light curve superposed: a broken power law and three Gaussian components describing the behaviour of flares. The red data points show the X-ray light curve, in units of count rate, fitted with a double broken power law, see Section 3.1 for the fit parameters.

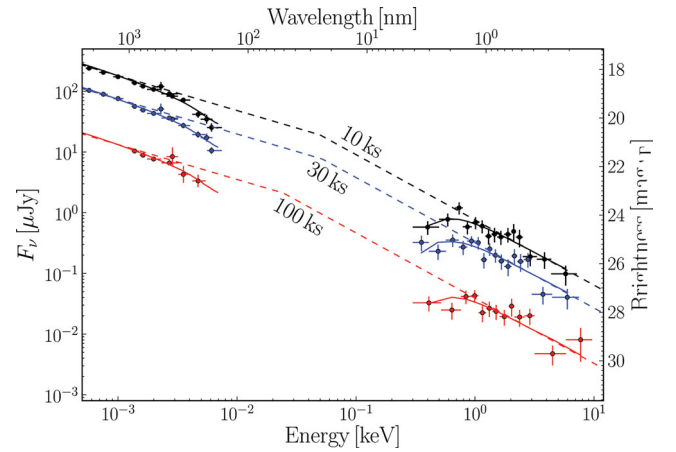


**Figure 11.** X-ray–optical spectral energy distributions at three epochs (observer frame). Fits are done with a broken power law with a fixed difference between the two power-law spectral indices, and with the same X-ray absorption and optical extinction for all three epochs.

for  $\nu > \nu_c$  it has the same index as for the homogeneous medium. The values for a homogeneous medium agree well with the values determined from the light curve fits (using the two-break model on the XRT data) for the pre-break slopes, and are consistent with the presence of a cooling break between X-ray and optical frequencies. In addition, in a wind-like medium the cooling break frequency should increase with time, which is not observed.

The break times in optical and X-rays are broadly in agreement, and the SEDs (Fig. 11; the first SED is before the break, the last after) show no evidence that the break is wavelength dependent (chromatic). As such, identifying this break with a jet break is compelling, particularly as this break is the second light curve break seen in the X-ray afterglow, with the first likely marking the end of energy injection. However, we note that the post-break decay indices ( $1.33 \pm 0.02$  and  $1.54 \pm 0.15$  for optical and X-rays, respectively) are too shallow compared to predictions from the standard fireball

model, both in the case of non-sideways spreading jets (which predicts post-break decay indices of  $1.52 \pm 0.11$  for optical and  $2.12 \pm 0.11$  for X-rays) and sideways spreading jets (which should give post-break decay indices of  $p$ ).

An alternative interpretation could be that the break is not a jet break, but rather a break marking the start of the ‘normal’ afterglow phase, i.e. the decay indices after this break are pre-jet break indices, and the phase before this break is dominated by energy injection. In this case the post-break optical index of  $1.33 \pm 0.02$  is consistent with the closure relations in the case of a wind medium, which predicts  $1.37 \pm 0.11$ . However, in that interpretation the optical decay index should be steeper than the X-ray one, and the predicted X-ray decay index of  $1.12 \pm 0.11$  is not consistent with the measurement.

We note that the homogeneous analyses of large samples of *Swift* XRT afterglows have shown that a large fraction of afterglows with candidate jet breaks (i.e. a light curve break significantly after a plateau phase) produce post-break decay indices that are too shallow compared to simple model predictions (Willingale et al. 2007; Evans et al. 2009, their fig. 10; and Racusin et al. 2009, their fig. 2). Both these papers further point out several additions to the models that can possibly explain some of this discrepancy, for example the presence of low-level continuous energy injection past the plateau phase, or peculiar jet structure and sightline configurations. In the following we will consider the observed break a candidate jet break, and will discuss alternative options as well.

If the break is a jet break, we can correct the isotropic energy  $E_{\text{iso}}$  for beaming. Using  $E_{\text{iso}} = 3.7 \times 10^{51}$  erg (Golenetskii et al. 2009) and making the same assumptions as in Kocevski & Butler (2008), we find a jet opening angle  $\theta_{\text{jet}} \sim 0.059$  rad, or  $3.4^\circ$ , leading to  $\log(E_\gamma) \sim 48.9$ . This is a fairly low value for  $E_\gamma$ , but not unprecedented: similar values are found for several other *Swift* bursts (Kocevski & Butler 2008) and pre-*Swift* bursts (Frail et al. 2001).

### 3.2 Circular polarization

The presence of a (weak) ordered magnetic field in addition to a chaotic, incoherent magnetic field generated by the post-shock turbulence has been proposed (e.g. Granot & Königl 2003) to explain the non-detection of the swing in the linear polarization position angle at the time of the jet break, expected in some models (e.g. Lazzati et al. 2003). In this picture, the observed polarization may be dominated by the weak large-scale ordered field, while emissivity is dominated by the random tangled field made by the post-shock turbulence. Polarization variability occurs as a result of changes in the ratio of the ordered to random mean-squared field amplitudes (Granot & Königl 2003). This results in much weaker changes in the polarization and polarization position angle light curve around the jet break time. A direct test of this proposition can come from deep circular polarization. Some searches have been performed at radio wavelengths during radio flares (Granot & Taylor 2005), but with fairly poor sensitivity (the best upper limit on circular polarization is 9 per cent for GRB 991216).

Our data set contains four measurements of circular polarization in optical, R-band, wavelengths, see Table 1, each with uncertainties of 0.15 per cent. Under the assumption that over the interval that the data were obtained ( $\sim 0.7$  h, see Table 1) there is no change in circular polarization, we can combine these together. We find a combined value of the circular polarization Stokes parameter of  $v = V/I = -0.00020 \pm 0.00075$ , which leads to a formal  $2\sigma$  upper limit of  $P_{\text{circ}} < 0.15$  per cent: the deepest limit on circular polarization of a GRB afterglow to date. Figs 4 and 6 show that during the circular polarimetry epoch, the optical light curve shows a low-amplitude

bump. As such, the limit on the circular polarization can be seen as a limit on the circular polarization of the light of the bump plus that of the underlying afterglow.

### 3.3 Interstellar polarization within the host galaxy

The variability of the detected linear polarization indicates that the majority of detected polarization can be associated with the afterglow. However, scattering of afterglow light on to dust grains within the host galaxy (host galaxy interstellar polarization – HGIP, following the terminology of Gorosabel et al. 2010) can induce noticeable linear polarization, depending on the dust scattering geometry and grain size distribution. This can affect attempts to interpret polarization behaviour around jet breaks (e.g. Lazzati et al. 2003) or models using the absolute level of polarization (e.g. Gruzinov & Waxman 1999; Gruzinov 1999). For example, the zero polarization seen in e.g. *lin1* could in principle be an unfortunate effect of HGIP on an intrinsically non-zero polarized afterglow.

We can utilize the reasonable assumption that over the optical range, the intrinsic afterglow linear polarization will be wavelength independent as it is synchrotron emission, whereas HGIP will be strongly wavelength dependent. In the Galactic ISM, the polarization broadly follows an (empirical) relation known as the Serkowski law (Serkowski 1973):

$$P_{\text{lin}} = P_{\text{lin,max}} \exp\left(K \ln^2\left(\frac{\lambda_{\text{max}}}{\lambda}\right)\right).$$

In this relation,  $P_{\text{lin,max}}$  is the maximum induced linear polarization at wavelength  $\lambda_{\text{max}}$ . The wavelength  $\lambda_{\text{max}}$  traces the size (distribution) of the dust grains responsible for the observed polarization, and as such is closely linked to  $R_V = A_V/E(B - V)$ . Klose et al. (2004) considered the effect of redshift in the Serkowski law, which results in a substitution  $\lambda_{\text{max}} \rightarrow (1+z)\lambda_{\text{max}}^{\text{host}}$  in the equation above, and the relation  $\lambda_{\text{max}}^{\text{host}} = R_V/5.5$ . Klose et al. (2004) derive the observed linear polarization  $P_{\text{lin}}/P_{\text{lin,max}}$  in standard photometric broad-band filters of an intrinsically unpolarized afterglow due to the presence of dust in the host, as a function of redshift  $z$  and  $R_V$ . Using the results in Klose et al. (2004), we generate predictions for observed  $P_{\text{lin}}/P_{\text{lin,max}}$  in several broad-band filters as a function of  $R_V$ , using  $z = 0.971$ , shown in Fig. 8. From these, a predicted ratio  $P_{\text{lin,R}}/P_{\text{lin,K}}$  is produced as a function of  $R_V$ , plotted in the lower panel of Fig. 8. Multi-wavelength linear polarimetry has been possible for only a small number of bursts: 020813 (Barth et al. 2003; Lazzati et al. 2004), 021004 (Lazzati et al. 2003) and 030329 (Greiner et al. 2003; Klose et al. 2004). In these cases, no significant evidence for HGIP has been observed.

Our *Ks*-band polarimetry is approximately simultaneous to the *R*-band polarimetry epoch *lin9* (to be exact, *lin9* is simultaneous with *linK3*). The (GIP-corrected) Stokes parameters for *lin9* and *linK* are very similar, though we caution that the data were taken during what appears to be a bump in the polarization light curve (Fig. 6). The resulting position angles are identical within errors, and we find  $P_{\text{lin,R}}/P_{\text{lin,K}} = 0.72 \pm 0.45$ . This, combined with the strong detected variation of both polarization degree and angle, demonstrates that (within errors) there is no indication of substantial HGIP contribution to the observed polarization. Martin & Angel (1976) demonstrate that the ISM induces a small degree of circular polarization even in unpolarized sources. However, the levels of induced circular polarization are an order of magnitude or more below the limit we set in Section 3.2, considering the measured Galactic GIP and the low extinction in the host galaxy (Section 3.1).

In the following we therefore proceed with the assumption that the GIP-corrected polarization is all intrinsic to the source. In a future paper (Paper 2) we will further quantify the implication of this measurement (and those of other GRB afterglows) on the dust and gas properties in GRB sightlines. A possibility that we will also address in Paper 2 is the effect of dust destruction by the GRB and afterglow high-energy radiation, which may make the effect of HGIP time dependent.

### 3.4 Linear polarization light curve

Our *R*-band linear polarimetric monitoring took place over three observing nights, as described in Section 2.1.1. The behaviour over the first two nights is illustrated in Figs 6 and 7, shown in linear time coordinate. On the third night only one deep, final, measurement was taken.

In the first night (see Fig. 6), the source starts off with very low (consistent with zero, within the errors dominated by the uncertainty in the GIP Stokes parameters) polarization, the lowest observed for a GRB afterglow to date. Following that, a broad, low-amplitude bump may be present in the polarimetric curve. GRBs 030329 and 021004 showed a correlation between linear polarization behaviour and light curve bumps (e.g. Greiner et al. 2003). In Fig. 6 we indicate the times of the three bumps we find in our data. Some variability may be present related to these bumps, but the statistical significance is very low. After the first eight data points obtained at the start of the night, observations were resumed at the end of the night, showing a decline from a higher polarization level (Table 2), confirmed by the ISAAC polarimetry taken quasi-simultaneous to *lin9*. Over the first night, some low-level variation in position angle may be present, but the uncertainties are large because of the low linear polarization: overall, the first night data are consistent with a constant polarization angle.

The second night data (see Fig. 7) display short time-scale variability: a polarization bump, peaking at  $\gtrsim 3$  per cent polarization, accompanied by a clear rotation of the position angle. Following this, the end of the night shows a slow rise in polarization, accompanied by further position angle variation. By the third night, the afterglow had become too faint for detailed sampling, and one deep data point, *lin20*, was obtained (Table 2). This last data point clearly shows low-level contribution from the host galaxy in the received light. We will attempt to interpret the polarimetric data in Section 4.

### 3.5 Environment of the burst

In a forthcoming paper on this data set (Paper 2) we will analyse the GRB environment in detail. In this section we will derive some properties most relevant to the afterglow physics, and to show that this burst displays no indications of being unusual.

In the late-time images taken with Gemini (see Table 3) the host galaxy can clearly be seen as an extended structure, see Fig. 12, visibly extended in the east–west direction. An isophote fit using elliptical isophotes (using the *ellipse* package within *IRAF*) gave a best fit for an ellipse orientation of  $89 \pm 4^\circ$ . We determined the position of the GRB within its host by performing image subtraction of the three Gemini epochs using a modified version of the *ISIS2* code (Alard & Lupton 1998). We detected a clear afterglow residual in a subtraction of the first and third epoch, and between the first and second epochs. No residual was detected in a subtraction between the second and third epochs. We found the GRB location to be offset by approximately 5.8 kiloparsec from the centre of the galaxy (as found from the elliptical isophote fits), see Fig. 12. This offset, as

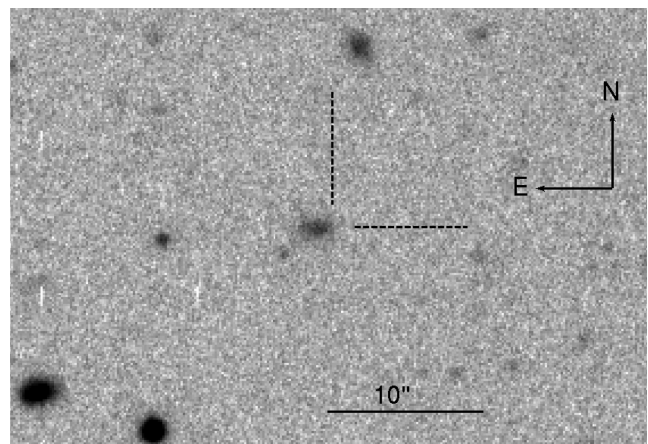


**Figure 12.** The host galaxy of GRB 091018, from the second epoch Gemini GMOS *r*-band data. The dashed tickmarks mark the position of the GRB as determined from PSF-matched image subtraction of Gemini epochs 1 and 2.

well as the observed host magnitude,  $r = 23.4$  (*AB*; see Table 3), is well within the observed distribution for long GRBs at this redshift (e.g. Bloom, Kulkarni & Djorgovski 2002; Savaglio, Glazebrook & LeBorgne 2009).

The X-shooter afterglow spectra show very strong absorption lines (Fig. 13) composed of at least three discrete velocity components, spanning  $\sim 300 \text{ km s}^{-1}$ . No lines from intervening systems are detected. At the GRB redshift we detect both common resonance lines and a small number of transitions arising from excited fine-structure and metastable levels (from Fe II and possibly Ni II), though the lines from these excited transitions are very weak in our spectrum. Time-resolved spectroscopy of GRB afterglows has shown that these excited transitions are excited through indirect UV pumping (fluorescence) by the afterglow photons (e.g. Vreeswijk et al. 2007). This unambiguously identifies the redshift  $z = 0.971$  to be that of the GRB.

The X-shooter spectra were taken with the slit position angle aligned with the parallactic angle, set at  $-90.8^\circ$  at the start of observations, and therefore oriented broadly along the host galaxy. In addition to absorption lines, we therefore also detect nebular emission lines in the spectrum (e.g. H  $\alpha$ , [O II], [O III]), though their signal to noise is low as the afterglow strongly dominates the light (see Table 3). The detection of the resolved [O II]  $\lambda\lambda 3726, 3729$  doublet is shown in Fig. 9. Its flux of  $\sim 6 \times 10^{-17} \text{ erg s}^{-1} \text{ cm}^{-2}$  can be used to derive an estimate of the star formation rate (SFR): using the equation from Kennicutt (1998) we find an SFR ([O II])  $\sim 4 M_\odot$  per year. If we instead use the empirical conversion from [O II] line luminosity to SFT derived by Savaglio et al. (2009) for GRB host galaxies, we find SFR ([O II])  $\sim 1.6 M_\odot$  per year (note that no extinction correction was applied to the [O II] line luminosity). This SFR ([O II]) is fairly typical for long GRB hosts (Savaglio et al. 2009). In conclusion, the afterglow spectrum, host magnitude and morphology, and star formation rate are all in line with expectations for a normal long GRB host galaxy.

In Paper 2 we will further analyse the spectrum and exploit the rare opportunity where we can probe (interstellar) gas and dust in the host galaxy using five methods simultaneously: through afterglow absorption lines (including excited fine-structure lines), nebular emission lines, afterglow SEDs, wavelength-dependent linear polarimetry and host imaging.



points of 030329, 021004 and 020813. It is clear that polarimetry very early after burst requires automated/robotic procedures. Using such an approach, a very early afterglow polarimetric detection of GRB 090102 was obtained by Steele et al. (2009), who secure a detection of  $P_{\text{lin}} = 10.2 \pm 1.3$  per cent at rest-frame time 75 s after burst, using the robotic Liverpool Telescope. Such a high degree of polarization, measured when the reverse shock component was still bright, is consistent with the presence of large-scale ordered magnetic fields. Although our data on 091018 are taken considerably later in time than those on 090102, the superb sensitivity of the VLT may allow us to continue to probe the magnetic field structure at late time through our high-precision linear and circular polarimetry.

## 4.2 GRB 091018 and models

### 4.2.1 Reverse shock

The start of our polarimetric monitoring was sufficiently late that a contribution of reverse shock emission to the received light is likely negligible. While this precludes study of some magnetization properties (e.g. Granot & Taylor 2005), this makes a comparison of the data with models easier, as only a forward shock model needs to be considered. The low linear polarization at the start of our monitoring appears to confirm this: emission from reverse shocks is expected to be considerably polarized, as the shock travels back into magnetized shocked material (e.g. Granot & Taylor 2005; Steele et al. 2009).

### 4.2.2 Jet break

We compare our data with the model series computed by Rossi et al. (2004), hereafter referred to as R04, who derive the expected linear polarization curves (including position angle) for a grid of different jet model parameters, assuming that there is no additional coherent component of the magnetic field present and that HGIP is negligible. In particular, R04 consider the cases of homogeneous jets, structured jets and Gaussian jets, each with a grid of different viewing angles (in the case of homogeneous jets this is the angle the line of sight makes with the jet axis), and for a range of wavelengths and physical parameters. They further distinguish jet breaks with and without sideways spreading.

We can briefly summarize the main differences between the various models as found by R04, and refer for details and explanations to that paper (see also fig. 18 of R04):

(i) Homogeneous jets show two peaks in the polarization curves, with the second peak always reaching a higher polarization than the first. Structured and Gaussian jets show one peak only, with peak time for a Gaussian jet significantly later than for a structured jet, which has its peak around the time of the break. The peaks of the structured and Gaussian jets are much wider than the ones for homogeneous jets (i.e. rise time and decay time-scales are long).

(ii) The position angle for a homogeneous jet changes by  $90^\circ$  in between the two peaks in the polarization curves: the two peaks each have constant position angle, but are  $90^\circ$  different. Structured and Gaussian jets have constant position angles throughout.

(iii) Structured jets show non-negligible polarization at early times, whereas homogeneous jets and Gaussian jets have zero polarization at early times.

(iv) The shape of the bumps in the different jet structures is different.

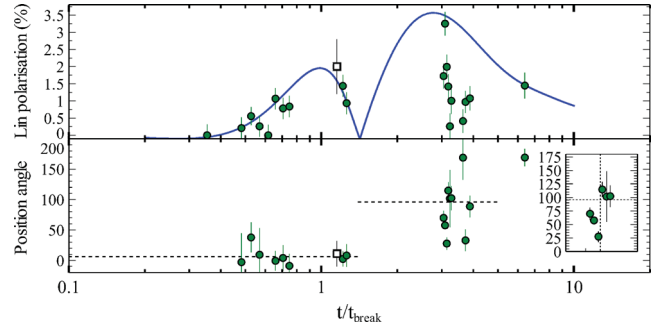


**Figure 14.** All GIP-corrected linear polarization data plotted as a function of the time since burst divided by the time of the break in the optical light curve (i.e.  $t_{\text{break}} = 3.23 \times 10^4$  s). Overplotted in blue is the model (from Rossi et al. 2004) for a homogeneous jet with a jet break at  $t_{\text{break}}$  that does not experience sideways expansion, with viewing angle  $\theta_{\text{obs}} = 0.2\theta_{\text{jet}}$ . The model has been shifted slightly (by dividing the model  $t/t_{\text{jet}}$  by 1.15). The lower panel shows the polarization position angle. The dotted line for  $t/t_{\text{jet}} < 1.5$  shows the average position angle ( $6^\circ$ ). The dotted line for  $t/t_{\text{jet}} > 1.5$  is set at  $96^\circ$ : the average value before this time plus  $90^\circ$ , to show the predicted  $90^\circ$  position angle swing. The inset shows the rapid polarization rotation at  $t/t_{\text{break}} \sim 3.16$  (vertical dotted line in the inset), with the horizontal dotted line at a position angle of  $96^\circ$ .

(v) Sideways expanding jets show lower polarization values than non-sideways expanding jets (all other parameters being equal), with wider bump(s) in the polarization curve.

We start by evaluating the data in time coordinates normalized by the time of the break seen in the optical data (see Section 3.1). It is clear that some polarization behaviour is observed occurring close to  $t/t_{\text{break}} \sim 1$ , as expected for jet breaks. In the case when this break is a jet break, we can then directly compare the curves with those in R04. Fig. 14 shows a plot in these units. Comparing to the points (i)–(v) listed above, there appears to be evidence that a model with constant position angle throughout will not provide a good fit; early-time polarization is consistent with zero (or at least is lower than predictions for structured jets); a single bump model with a shape as predicted by the models in R04 seems inconsistent with the data. In Fig. 14 we therefore plot a model for a homogeneous, non-sideways expanding jet with viewing angle  $\theta_{\text{obs}} = 0.2\theta_{\text{jet}}$  (from fig. 8 in R04). We shift this curve slightly in time coordinate by dividing  $t/t_{\text{jet}}$  by 1.15 to get a better visual match. The first bump in the polarization curve appears to be well reproduced in both shape and amplitude, including the zero polarization at early times. This model predicts a constant polarization position angle over the first bump. We indicate in Fig. 14 (dotted line) the average of the position angle at  $t/t_{\text{break}} \lesssim 1.4$ . As required by the R04 model, the position angle is constant over this bump.

The second bump predicted by the homogeneous jet model should have a larger amplitude than the first, a position angle  $90^\circ$  offset from the first bump and a morphology opposite to the first (in coordinates used in Fig. 14). Some of the data points indeed have a higher polarization than seen in the first bump, but the morphology of the bump as predicted by the model is not observed. We examine the behaviour of the position angle by adding  $90^\circ$  to the position angle for  $t/t_{\text{break}} \lesssim 1.4$ . In Fig. 14 this is the second horizontal dotted line. It is clearly seen that the value of the position angle is overall higher than in the first bump, but is not constant as the model predicts, showing considerable variability on a short time-scale (possibly varying around the predicted position angle), including a rotation of the position angle visible in the interval  $t/t_{\text{break}} \sim 3.0$ – $3.3$ . The

polarization curve shows, compared to the homogeneous jet model, a deep short dip, in the interval  $t/t_{\text{break}} \sim 3\text{--}4$ . This dip shows a very steep decay in the first few data points, simultaneous with the observed rotation in position angle. This behaviour is not predicted by any jet break model.

We could consider the possibility that there is an additional polarization curve component (hereafter simply referred to as the extra component) on top of a slower behaviour as predicted by jet break models. A third smooth, fairly narrow, polarized bump peaking at around  $t/t_{\text{break}} \sim 3\text{--}4$  could be present, having a position angle significantly offset from the  $\theta = 96^\circ$  of the second bump from the homogeneous jet model. The sum of this component and that of the (second bump of the homogeneous) jet model can give rise to most of the observations: the steep dip, where the contributions of the two components nearly cancel due to differing position angles, and the rotation in position angle, where the components are at similar amplitude but very different position angle. However, this is a rather degenerate problem, as the amplitude as a function of time (the shape) of the extra component and the position angle as a function of time are all unknown. A component with a fixed position angle but variable amplitude (i.e. a component much like the polarization peaks from a jet break) can approximate the data (with a position angle  $\sim 70^\circ$  offset from the constant  $96^\circ$ , and peaking around  $t/t_{\text{break}} \sim 3.5$ ), but a component with nearly constant amplitude but position angle varying on very short time-scales can provide a reasonable approximation too. Wu et al. (2005) evaluate the expected polarization curves of afterglows from two-component jets (as proposed for e.g. 030329, Berger et al. 2003), which show, as expected, a large variety of behaviour, depending mostly on viewing angle and contrast between the narrow and wide jet components. However, the observed variability in the data of 091018 around  $t/t_{\text{break}} \sim 3\text{--}4$  is much more rapid than predicted by the models of Wu et al. (2005). At the current data quality, and including the uncertainty in and applicability of the underlying model (homogeneous jet model from R04), we are not in a position to quantify the behaviour of this putative component further. As the shape of the bump and time variability of the position angle are unclear, it is difficult to speculate on the possible origin of such an additional component. The feature occurs after the expected time of the peak of the second bump in the R04 model and no such feature is visible at  $t < t_{\text{break}}$ . As such, it may be related to a discrete bright region (patch) on the jet that comes into view just after the second bump peaks. In this scenario we may expect a constant position angle of the component produced by the patch (if the field in the patch is coherent), with a bump shape reflecting the brightness profile of the bright patch. However, other explanations, such as microlensing, two-component jets or others, are difficult to rule out with the polarization data alone.

The time-span possibly most affected by the extra component,  $t/t_{\text{break}} \sim 3\text{--}4$ , corresponds to  $9.7\text{--}12.9 \times 10^4$  s. In the optical light curves no significant slow variability at around that time is obvious. The XRT data show a possible broad, slow softening around this time, but our SED fits do not point to strong spectral variation at this time. The shallow post-break decay indices and/or the flares observed in the optical light curve (Section 3.1) may be related to the observed polarization behaviour, i.e. be linked to the observed extra component, but further modelling will be required to test this.

There is at least one other source that shows a variability in the polarization curve on short time-scales (intranight) and unrelated to a jet break, GRB 020405. However, in that source only a single data point showed the deviation from a constant polarization degree (Bersier et al. 2003a), and the position angle was not seen

to vary over the available polarization measurements. No features resembling jet break bumps were detected in that source, consistent with the absence of a jet break in the light curves. The possible detection of a variation at fairly short time-scales, with possibly a constant position angle and likely unrelated to a jet break in GRB 091018 (the extra component in the polarization curve) may be an indication that this type of behaviour is indeed real.

The conclusion from the above discussion is that none of the simple models of polarization behaviour of GRBs directly reproduces the observed behaviour. Of the available models, the homogeneous jet break model comes closest, but requires at least one additional component, the nature of which is currently unknown.

#### 4.2.3 Ordered fields

The circular polarization upper limit derived in Section 3.2 can be used to probe large-scale ordered fields, which have been proposed by several authors to explain various phenomena, such as the high linear polarization at very early times (Steele et al. 2009), or the lack of obvious polarization position angle shifts around the jet break time for e.g. GRBs 030329 and 021004 (Granot & Königl 2003). Models of the expected circular polarization in optical wavelengths for an external shock (Matsumiya & Ioka 2003; Sagiv et al. 2004; Toma, Ioka & Nakamura 2008) generally find that afterglows should show very low circular polarization in the absence of strong large-scale ordered fields. Our detection limit of  $P_{\text{circ}} < 0.15$  per cent is in full agreement with these predictions (see e.g. Toma et al. 2008) and excludes strong ordered field components. We note the timing of our circular polarimetry: our data were taken when the reverse shock emission is likely negligible, and when the linear polarization was still very weak. It is clear that it is not easy to significantly improve on the depth of this limit in optical wavelengths, but it would be interesting to search for circular polarization in other bursts, to establish whether this is a common feature, and to search for circular polarization at early times when reverse shock emission is still present.

#### 4.2.4 Energy injection

An alternative explanation of the observed break in the light curves is that this break marks the end of (continuous) energy injection, though the post-break decay indices are not as expected from the closure relations (Section 3.1). The occurrence of significant polarimetric variability at around  $t/t_{\text{break}} \sim 1$  indicates that if this scenario is correct, the end of energy injection must be accompanied by a geometric change, as the polarization position angle stays constant. In a study of GRB 021004, Björnsson, Gudmundsson & Jóhannesson (2004) model the strong rebrightenings visible in the afterglow light curve with discrete, powerful, energy injections and demonstrate that the light curves are fairly well reproduced this way. They demonstrate that their model shows some correlation with the polarimetric data, i.e. that polarization is related to bumps. For GRB 030329, Greiner et al. (2003) come to a similar conclusion from their data. We see at least three low-amplitude bumps in the optical light curve, at times given in Section 3.1, but a correlation with polarimetric behaviour is not clearly visible, largely because of the larger uncertainties in our polarization values compared to the much brighter afterglow of 030329. Similarly, a possible relation between the extra component in the polarization curve and the flaring around the jet break time is unclear. Future (numerical) models of light curve bumps/flares (e.g. Vlasov et al. 2011) and high-quality

data (e.g. Krühler et al. 2009) may provide the possibilities of computing expected polarization signals from the simulations. These may then be used to understand the connection between the physical parameters behind these bumps and the behaviour in polarized light.

## 5 CONCLUSIONS

We presented a large polarimetry data set of the afterglow of GRB 091018, and add to that an extensive multicolour photometric data set and medium resolution spectroscopy. We find an abundance of absorption lines in the spectrum of the afterglow as well as a few emission lines, from which we find a redshift  $z = 0.971$ . The X-ray light curve shows at least two breaks, as well as a complex of flaring activity. The densely sampled optical light curve shows several flares as well, and through a fit using a broken power law and three Gaussian components (to describe the flares), we find an achromatic break at  $t_{\text{break}} \sim 3.2 \times 10^4$  s. Our polarization data cover this break, allowing us to probe its nature using linear polarimetry. Our polarimetry results can be summarized as follows.

- (i) In contrast to GRBs 030329 and 021004, there are no strong rebrightenings that confuse our view of the polarization behaviour.
- (ii) Our deep circular polarimetry at  $t \sim 0.15$  d after burst shows no circular polarization, with  $2\sigma$  limit  $P_{\text{circ}} < 0.15$  per cent.
- (iii) The quasi-simultaneous  $R$ - and  $K_s$ -band polarimetry shows no strong indications of a considerable contribution of polarization from the ISM in the host galaxy.
- (iv) The linear polarimetry shows a constant position angle for  $t/t_{\text{break}} < 1.4$ , and a considerably higher, but strongly variable, value thereafter.
- (v) At least two peaks are present in the polarization curve. The first of these, as well as the constant position angle, is well reproduced by a model of a jet break using a homogeneous, non-sideways spreading jet with small viewing angle (from R04).
- (vi) If the observed break is a jet break, and if the model of a homogeneous, non-sideways spreading jet is correct, an additional component is required to reproduce the observed polarization curve and position angles. This may be a short-duration bump with constant position angle, offset from the position angle of the underlying jet break component.

From the above it is clear that the models for polarization behaviour around the time of jet break (as in R04) cannot, in their current form and on their own, explain the full behaviour of the polarization curve of 091018. Further modelling efforts, in particular into the effects of rebrightenings/bumps and continuous energy injection on the observed polarization, are vital to exploit the full potential of polarimetry as probe of afterglow physics.

These results are the first of their kind for *Swift* GRBs, and indeed GRB 091018 can be considered a ‘normal’ GRB, with none of its prompt emission or afterglow properties particularly remarkable, in contrast to some of the polarimetrically studied pre-*Swift* bursts like 030329. This is in part because our selection criteria of sources to study with polarimetry were only that: the source had to be a *Swift* burst with a detected afterglow in both XRT and UVOT data. This avoids a bias towards the brightest or slowest decaying optical afterglows, and indeed it is clear from Section 3.1 that GRB 091018 is one of the faintest afterglows with multi-night polarimetry. Further, similar observations of (*Swift*) bursts with different micro- and macro-physical parameters (in particular energetics, jet opening angle, density  $n$  and density gradient  $k$ ) will be required to establish

whether or not GRB 091018 is representative of the sample of GRB afterglows as a whole.

Unfortunately, no long-wavelength (radio, (sub-)mm) observations were available for GRB 091018. A deep polarimetric campaign on an afterglow, with radio and (sub-)mm light curve data in addition to optical and X-ray light curves, would be particularly interesting, since with the resulting broad-band SEDs (with sensitivity redwards of the synchrotron peak frequency  $\nu_m$ ) we would be able to fit for parameters that are particularly relevant for polarimetric interpretations, e.g.  $\epsilon_E$  and  $\epsilon_B$ .

## ACKNOWLEDGMENTS

We warmly thank the ESO staff for obtaining the VLT data discussed here. We thank Justyn Maund, Dave Russell, Daniele Malesani, Piergiorgio Casella, Elena Rossi, Christina Thöne and Alexander Kann for their help and useful discussions. We thank the anonymous referee for useful comments and suggestions. Based on observations made with ESO Telescopes at the Paranal Observatory under programmes 084.D-0949 and 084.A-0260. KW acknowledges support from STFC. TK acknowledges support by the European Commission under the Marie Curie Intra-European Fellowship Programme. The Dark Cosmology Centre is funded by the Danish National Research Foundation. RLCS is supported by a Royal Society Fellowship. The financial support of the British Council and Platform Beta Techniek through the Partnership Programme in Science (PPS WS 005, PI: Wiersema) is gratefully acknowledged. Part of the funding for GROND (both hardware as well as personnel) was generously granted from the Leibniz-Prize to Prof. G. Hasinger (DFG grant HA 1850/28-1). SK and AR acknowledge support by DFG grant KI 766/16-1, and AR in addition from the BLANCEFLOR Boncompagni-Ludovisi, née Bildt foundation. This work made use of data supplied by the UK *Swift* Science Data Centre at the University of Leicester. IRAF is distributed by the National Optical Astronomy Observatory, which is operated by the Association of Universities for Research in Astronomy (AURA) under cooperative agreement with the National Science Foundation.

## REFERENCES

- Alard C., Lupton R. H., 1998, *ApJ*, 503, 325
- Barth A. et al., 2003, *ApJ*, 584, 57
- Berger E. et al., 2003, *Nat.*, 426, 54
- Bersier D. et al., 2003a, *ApJ*, 583, L63
- Bersier D. et al., 2003b, *ApJ*, 584, L43
- Björnsson G., Gudmundsson E. H., Jóhannesson G., 2004, *ApJ*, 615, L77
- Bloom J. S., Kulkarni S. R., Djorgovski S. G., 2002, *AJ*, 123, 1111
- Bloom J. S., van Dokkum P. G., Baily C. D., Buxton M. M., Kulkarni S. R., Schmidt B. P., 2004, *AJ*, 127, 252
- Burenin R. A. et al., 2003, *Astron. Lett.*, 29, 573
- Cardelli J. A., Clayton G. C., Mathis J. S., 1989, *ApJ*, 345, 245
- Chandrasekhar S., 1960, *Radiative Transfer*. Dover, New York
- Chen H.-W. et al., 2009, *GCN Circ.* 10038
- Costa E. et al., 1997, *Nat.*, 387, 783
- Covino S. et al., 2003, *A&A*, 400, L9
- Curran P. A. et al., 2007a, *MNRAS*, 381, 65
- Curran P. A. et al., 2007b, *A&A*, 467, 1049
- Cushing M. C., Vacca M. D., Rayner J. T., 2004, *PASP*, 116, 362
- Evans P. A. et al., 2009, *MNRAS*, 397, 1177
- Filgas R., Krühler T., Yoldaş A., Klose S., Greiner J., 2009, *GCN Circ.* 10039
- Fossati L., Bagnulo S., Mason E., Landi Degl’Innocenti E., 2007, in Sterken C., ed., *ASP Conf. Ser.*, Vol. 364, *The Future of Photometric*,

- Spectrophotometric and Polarimetric Standardization. Astron. Soc. Pac., San Francisco, p. 503
- Fox D. W. et al., 2003, *Nat*, 422, 284
- Frail D. A. et al., 2001, *ApJ*, 562, L55
- Gehrels N. et al., 2004, *ApJ*, 611, 1005
- Gehrels N., Ramirez-Ruiz E., Fox D. B., 2009, *ARA&A*, 47, 567
- Ghisellini G., Lazzati D., 1999, *MNRAS*, 309, L7
- Goldoni P., Royer F., François P., Horrobin M., Blanc G., Vernet J., Modigliani A., Larsen J., 2006, *SPIE*, 6269, 80
- Golenetskii S. et al., 2009, *GCN Circ.* 10045
- Gorosabel J. et al., 2010, *A&A*, 522, 14
- Granot J., Königl A., 2003, *ApJ*, 594, L83
- Granot J., Taylor G. B., 2005, *ApJ*, 625, 263
- Greiner J. et al., 2003, *Nat*, 426, 157
- Greiner J. et al., 2008, *PASP*, 120, 405
- Greiner J. et al., 2011, *A&A*, 534, 108
- Gruzinov A., 1999, *ApJ*, 525, L29
- Gruzinov A., Waxman E., 1999, *ApJ*, 511, 852
- Holland S. T. et al., 2003, *AJ*, 125, 2291
- Joos F., Buenzli E., Schmid H. M., Thalmann C., 2008, *SPIE*, 7016, 70161I-1
- Kennicutt R. C., 1998, *ARA&A*, 36, 189
- Klose S., Palazzi E., Masetti N., Stecklum B., Greiner J., Hartmann D. H., Schmid H. M., 2004, *A&A*, 420, 899
- Kocevski D., Butler N., 2008, *ApJ*, 680, 531
- Kouveliotou C., Meegan C. A., Fishman G. J., Bhat N. P., Briggs M. S., Koshut T. M., Paciesas W. S., Pendleton G. N., 1993, *ApJ*, 413, L101
- Krühler T. et al., 2009, *ApJ*, 697, 758
- Krühler T. et al., 2011, *A&A*, 534, 108
- LaCluyze A. et al., 2009, *GCN Circ.* 10061
- Lazzati D., 2006, *New J. Phys.*, 8, 131
- Lazzati D. et al., 2003, *A&A*, 410, 823
- Lazzati D. et al., 2004, *A&A*, 422, 121
- Lipkin Y. M. et al., 2004, *ApJ*, 606, 381
- Markwardt C. B. et al., 2009, *GCN Circ.* 10040
- Martin P. G., Angel J. R. P., 1976, *ApJ*, 207, 126
- Martin P. G., Whittet D. C. B., 1990, *ApJ*, 357, 113
- Masetti N. et al., 2003, *A&A*, 404, 465
- Matheson T. et al., 2003, *ApJ*, 582, L5
- Matsumiya M., Ioka K., 2003, *ApJ*, 595, L25
- Mészáros P., Rees M. J., 1992, *MNRAS*, 257, 29
- Mészáros P., Rees M. J., 1997, *ApJ*, 476, 232
- Mirabal N. et al., 2003, *ApJ*, 595, 935
- Mundell C. G. et al., 2007, *Sci*, 315, 1822
- Nousek J. et al., 2006, *ApJ*, 642, 389
- Pandey S. B. et al., 2003, *Bull. Astron. Soc. India*, 31, 19
- Patat F., Romaniello M., 2006, *PASP*, 118, 146
- Piran T., Fan Y.-Z., 2007, *Phil. Trans. R. Soc. A.*, 365, 1151
- Racusin J. L. et al., 2009, *ApJ*, 698, 43
- Rhoads J. E., 1997, *ApJ*, 487, 1
- Rhoads J. E., 1999, *ApJ*, 525, 737
- Rol E. et al., 2003, *A&A*, 405, L23
- Roming P. W. A. et al., 2005, *Space Sci. Rev.*, 120, 95
- Rossi E. M., Lazzati D., Salmonson J. D., Ghisellini G., 2004, *MNRAS*, 354, 86 (R04)
- Sagiv A., Waxman E., Loeb A., 2004, *ApJ*, 615, 366
- Sari R., 1999, *ApJ*, 524, 43
- Sari R., Piran T., Halpern J. P., 1999, *ApJ*, 519, L17
- Sato R. et al., 2003, *ApJ*, 599, L9
- Savaglio S., Glazebrook K., LeBorgne D., 2009, *ApJ*, 691, 182
- Schady P. et al., 2012, *A&A*, 537, 15
- Serkowski K., 1973, in Greenberg J. M., van de Hulst H. C., eds, *IAU Symp.* 52. *Interstellar Dust and Related Topics*. Reidel, Dordrecht, p. 145
- Serkowski K., Matheson D. L., Ford V. L., 1975, *ApJ*, 196, 261
- Simmons J. F. L., Stewart B. G., 1985, *A&A*, 142, 100
- Sparks W. B., Axon D. J., 1999, *PASP*, 111, 1298
- Stamatikos M. et al., 2009, *GCN Circ.* 10034
- Steele I. A., Mundell C. G., Smith R. J., Kobayashi S., Guidorzi C., 2009, *Nat*, 462, 767
- Toma K., Ioka K., Nakamura T., 2008, *ApJ*, 673, L123
- Uemura M. et al., 2003, *Nat*, 423, 843
- Ukwatta T. N. et al., 2012, *MNRAS*, 419, 614
- Van der Horst A. J. et al., 2008, *A&A*, 480, 35
- van Paradijs J. et al., 1997, *Nat*, 386, 686
- Vlasis A., van Eerten H. J., Meliani Z., Keppens R., 2011, *MNRAS*, 415, 279
- Vreeswijk P. M. et al., 2007, *A&A*, 468, 83
- Wardle J. F. C., Kronberg P. P., 1974, *ApJ*, 194, 249
- Wiersema K., 2011, *MNRAS*, 414, 2793
- Wijers R. A. M. J., Galama T. J., 1999, *ApJ*, 523, 177
- Willingale R. et al., 2007, *ApJ*, 662, 1093
- Witzel G. et al., 2011, *A&A*, 525, 130
- Wu X. F., Dai Z. G., Huang Y. F., Lu T., 2005, *MNRAS*, 357, 1197

This paper has been typeset from a  $\text{\TeX}/\text{\LaTeX}$  file prepared by the author.